

FIXED FREQUENCY SERIES-PARALLEL DC/DC  
RESONANT CONVERTERS

CENTRE FOR NEWFOUNDLAND STUDIES

**TOTAL OF 10 PAGES ONLY  
MAY BE XEROXED**

(Without Author's Permission)

PANKAJ JAIN







# Fixed Frequency Series-Parallel DC/DC Resonant Converters

By

©Pankaj Jain

A thesis submitted to the School of Graduate Studies  
in partial fulfillment of the requirements for the degree of  
Master of Engineering  
Faculty of Engineering and Applied Science  
Memorial University of Newfoundland  
January, 1993

St. John's

Newfoundland

Canada



National Library  
of Canada

Acquisitions and  
Bibliographic Services Branch

395 Wellington Street  
Ottawa, Ontario  
K1A 0N4

Bibliothèque nationale  
du Canada

Direction des acquisitions et  
des services bibliographiques

395, rue Wellington  
Ottawa (Ontario)  
K1A 0N4

Your Mr. Votre adresse

Our Mr. Notre adresse

The author has granted an irrevocable non-exclusive licence allowing the National Library of Canada to reproduce, loan, distribute or sell copies of his/her thesis by any means and in any form or format, making this thesis available to interested persons.

The author retains ownership of the copyright in his/her thesis. Neither the thesis nor substantial extracts from it may be printed or otherwise reproduced without his/her permission.

L'auteur a accordé une licence irrévocable et non exclusive permettant à la Bibliothèque nationale du Canada de reproduire, prêter, distribuer ou vendre des copies de sa thèse de quelque manière et sous quelque forme que ce soit pour mettre des exemplaires de cette thèse à la disposition des personnes intéressées.

L'auteur conserve la propriété du droit d'auteur qui protège sa thèse. Ni la thèse ni des extraits substantiels de celle-ci ne doivent être imprimés ou autrement reproduits sans son autorisation.

ISBN 0-315-82601-0

Canada

## Abstract

This thesis presents generalized modeling and analysis of constant frequency dc/dc resonant converters taking into account the effect of transformer leakage reactance. Frequency-domain analysis is used to obtain generalized equations to describe the steady-state characteristics of the series-parallel resonant converters with primary and tertiary resonance. Transient analysis using state-space method is also presented for the primary-side resonant converter. Simulation results showing the effect of the leakage reactance of the high frequency transformer on the performance of these converters are presented. Experimental results to verify the model and simulation results are also provided. A model is developed for a series-parallel resonant converter with integrated magnetics which is suggested for further size reduction in the converter. A design example is provided to illustrate the use of the generalized equations and performance curves.

It is shown that the transformer leakage inductance has a significant effect on the operation of the converter and hence cannot be neglected in the design of the converter. It is also shown that a series-parallel resonant converter with tertiary resonance is more suitable for operation at higher frequencies.

## Acknowledgement

I wish to thank Dr. John E. Quicoe for his invaluable guidance, advice and financial support. I extend my thanks to the Faculty of Engineering and Applied Science for providing the financial support in the form of Graduate Fellowship and Teaching Assistantships. I also wish to thank all my professors, particularly Dr. Cecilia Moloney, for making my stay here more rewarding. A special thanks goes to the Power Group at Bell-Northern Research for allowing me to use their facility at Corkstown, Ottawa, to conduct experiments and providing technical support.

Finally, I thank all my colleagues and friends for the useful discussions, suggestions and the moral support without which this thesis would have been very difficult if not impossible.

# Contents

<b>Abstract</b>	<b>ii</b>
<b>Acknowledgement</b>	<b>iii</b>
<b>Contents</b>	<b>iv</b>
<b>List of Figures</b>	<b>vii</b>
<b>List of Tables</b>	<b>xiii</b>
<b>1 Introduction</b>	<b>1</b>
1.1 PWM dc/dc converters . . . . .	2
1.2 Resonant dc/dc converters . . . . .	3
1.2.1 Series resonant converters . . . . .	4
1.2.2 Parallel resonant converters . . . . .	7
1.2.3 Series-parallel resonant converter . . . . .	8
1.2.4 Control methods . . . . .	9
1.3 Thesis objective . . . . .	10
1.4 Thesis outline . . . . .	12
<b>2 Series-Parallel Resonant Converter With Primary Side Resonance</b>	<b>13</b>

2.1	Circuit description . . . . .	14
2.2	Frequency-domain model . . . . .	15
2.3	Steady-state analysis of the converter . . . . .	16
2.3.1	Assumptions . . . . .	17
2.3.2	Frequency-domain analysis . . . . .	18
2.3.3	Normalization . . . . .	20
2.3.4	Solution of equations . . . . .	22
2.4	Steady-state performance . . . . .	25
2.4.1	Simulated waveforms . . . . .	26
2.4.2	Effect of various parameters on the output voltage of the converter . . . . .	27
2.4.3	$\delta_{\min}$ vs. $K_p$ . . . . .	34
2.4.4	Resonant current $i_s$ vs. $K_p$ . . . . .	35
2.4.5	Inverter input current harmonics vs. $\delta$ . . . . .	37
2.4.6	Output voltage harmonics vs. commutation angle $\mu$ . . . . .	38
2.4.7	Total harmonic distortion in output voltage . . . . .	44
2.5	Transient analysis . . . . .	45
2.5.1	Analysis . . . . .	46
2.5.2	Simulation results . . . . .	50
<b>3</b>	<b>Series-Parallel Resonant Converter with Tertiary Winding Reso-</b>	
	<b>nance</b> . . . . .	<b>55</b>
3.1	Circuit description . . . . .	55
3.2	Frequency-domain model . . . . .	57
3.3	Steady-state analysis of the converter . . . . .	57
3.3.1	Frequency-domain analysis . . . . .	59

3.3.2	Solution of equations . . . . .	61
3.4	Steady-state performance . . . . .	64
3.5	Series-parallel resonant converter with integrated magnetics . . . . .	74
<b>4</b>	<b>Design Example and Experimental Results</b>	<b>78</b>
4.1	Design example . . . . .	78
4.2	Experimental results . . . . .	83
4.2.1	Primary resonant converter . . . . .	84
4.2.2	Tertiary side resonant converter . . . . .	99
<b>5</b>	<b>Conclusion</b>	<b>110</b>
5.1	Summary . . . . .	110
5.2	Recommendations for further research . . . . .	112
	<b>References</b>	<b>113</b>

# List of Figures

1.1	Simplified pulse-width modulated dc/dc converter topology . . . . .	2
1.2	Block diagram of a dc/dc resonant converter . . . . .	3
1.3	Basic circuit of a series resonant converter . . . . .	5
1.4	Basic configuration of a parallel resonant converter with isolation transformer . . . . .	7
1.5	Basic series-parallel resonant converter . . . . .	9
2.1	Circuit diagram of the dc/dc resonant converter . . . . .	15
2.2	Simplified circuit of the dc/dc resonant converter . . . . .	16
2.3	$n$ th harmonic equivalent circuit of the converter . . . . .	17
2.4	Generalized waveforms of the dc/dc resonant converter . . . . .	18
2.5	Equivalent circuit during the commutation period, $\mu$ . . . . .	23
2.6	Simulated waveforms of the converter for tuned series and parallel branches . . . . .	27
2.7	Simulated waveforms of the converter with $K_I = 4$ . . . . .	28
2.8	Simulated waveforms of the converter for inductive parallel branch . . . . .	28
2.9	Simulated waveforms of the converter for capacitive parallel branch . . . . .	29
2.10	Simulated waveforms of the converter for inductive series branch . . . . .	29
2.11	Simulated waveforms of the converter for capacitive series branch . . . . .	30
2.12	Simulated waveforms of the converter for reduced $\delta$ . . . . .	30

2.13	Output voltage $V_o$ vs. leakage reactance for $K_s = 0.6, 1.0$ and $1.4$ and $K_p \approx 1$ . . . . .	31
2.14	$V_o$ vs. switching frequency $f_s$ for different values of $K_s$ , and $K_p \approx 1$ . . . . .	31
2.15	$V_o$ vs. $\delta$ for different values of $X_L$ , and $K_p \approx 1$ . . . . .	33
2.16	$V_o$ vs. $\delta$ for different values of $K_s$ , and $X_L = 0.12$ . . . . .	33
2.17	$V_o$ vs. load resistance $R_l$ for different values of $K_s$ , and $K_p \approx 1$ . . . . .	34
2.18	$V_o$ vs. load resistance $R_l$ for $K_p = 2$ . . . . .	35
2.19	Variation of $\delta_{min}$ with $K_p$ for different values of $X_L$ , and $K_s = 1$ . . . . .	36
2.20	Variation of $\delta_{min}$ with $K_p$ for different values of $X_{cp}$ . . . . .	36
2.21	Variation of $i_s$ with $K_p$ for different values of $X_{cp}$ and $K_s = 1$ . . . . .	37
2.22	Variation of input current harmonics with $\delta$ for tuned series and parallel branches, $K_p \approx 1$ . . . . .	38
2.23	Variation of input current harmonics with $\delta$ for capacitive series branch, $K_p \approx 1$ . . . . .	39
2.24	Variation of input current harmonics with $\delta$ for inductive series branch, $K_p \approx 1$ . . . . .	39
2.25	Variation of input current harmonics with $\delta$ for inductive parallel branch, $K_s = 1$ . . . . .	40
2.26	Variation of input current harmonics with $\delta$ for capacitive parallel branch, $K_s = 1$ . . . . .	40
2.27	Variation of output voltage harmonics with $\mu$ for tuned series and parallel branches . . . . .	41
2.28	Variation of output voltage harmonics with $\mu$ for inductive series branch . . . . .	41
2.29	Variation of output voltage harmonics with $\mu$ for capacitive series branch . . . . .	42

2.30	Variation of output voltage harmonic, with $\mu$ for capacitive parallel branch . . . . .	42
2.31	Total harmonic distortion with $X_{Lr}$ , and $K_p \approx 1$ . . . . .	43
2.32	Total harmonic distortion with $K_I$ for capacitive series branch, and $K_p \approx 1$ . . . . .	43
2.33	Total harmonic distortion with $K_I$ for tuned series branch . . . . .	44
2.34	Different modes of operation of the converter . . . . .	46
2.35	Equivalent circuits for the four modes of operations . . . . .	47
2.36	Transient waveforms for first few cycles of operation with $K_p = 2$ . . . . .	52
2.37	Transient waveforms after ten cycles of operation with $K_p = 2$ . . . . .	52
2.38	Transient waveforms after twenty cycles of operation with $K_p = 2$ . . . . .	53
2.39	Transient waveforms for first few cycles of operation with $K_p \approx 1$ . . . . .	53
2.40	Transient waveforms after ten cycles of operation with $K_p \approx 1$ . . . . .	54
2.41	Transient waveforms at the end of thirty cycles of operation with $K_p \approx 1$ . . . . .	54
3.1	Circuit diagram of the dc/dc resonant converter . . . . .	56
3.2	$n$ th harmonic equivalent circuit of the converter . . . . .	58
3.3	Generalized waveforms of the dc/dc resonant converter . . . . .	59
3.4	Equivalent circuit during the commutation period $\mu$ . . . . .	62
3.5	Simulated waveforms of the converter for tuned series and parallel branch, $\delta = 114^\circ$ . . . . .	65
3.6	Simulated waveforms of the converter for tuned series and parallel branches, $\delta = 65^\circ$ . . . . .	65
3.7	Simulated waveforms of the converter for inductive parallel branch . . . . .	66
3.8	Simulated waveforms of the converter for capacitive parallel branch . . . . .	66
3.9	Simulated waveforms of the converter for inductive series branch . . . . .	67

3.10 Simulated waveforms of the converter for capacitive series branch . . .	67
3.11 Output voltage $V_o$ vs. leakage reactance for tuned series branch . . .	68
3.12 $V_o$ vs. switching frequency, $f_s$ . . . . .	69
3.13 $V_o$ vs. load resistance $R_l$ with tuned parallel branch . . . . .	70
3.14 $V_o$ vs. load resistance $R_l$ with capacitive parallel branch . . . . .	70
3.15 Resonant current, $i_s$ vs. $K_p$ for different values of $X_{cp}$ . . . . .	71
3.16 Variation of $\delta_{\min}$ with $K_p$ for different values of $X_{cp}$ . . . . .	72
3.17 Total harmonic distortion with $X_{ls}$ with tuned series and parallel branch	72
3.18 Total harmonic distortion with $K_l$ for $K_s=0.6, 1.0$ and $1.4$ for tuned parallel branch . . . . .	73
3.19 Total harmonic distortion with $K_l$ for $K_p=0.5, 1$ and $2.0$ . . . . .	73
3.20 $n$ th harmonic equivalent circuit for an integrated series-parallel reso- nant converter . . . . .	75
3.21 Simulated waveforms for a converter with integrated magnetics, $\delta = 114^\circ$	76
3.22 Simulated waveforms for a converter with integrated magnetics, $\delta = 65^\circ$	77
4.1 Output voltage, $V_o$ vs. $\delta$ . . . . .	82
4.2 Experimental setup for the series-parallel resonant converter with pri- mary resonance . . . . .	83
4.3 Efficiency with load for $V_i = 40V$ and $60V$ . . . . .	87
4.4 Simulated phase-shift modulated input voltage, $v_s$ for $V_i = 40V$ and $\delta = 175^\circ$ . . . . .	88
4.5 Experimental PSM input voltage, $v_s$ for $V_i = 40V$ . . . . .	88
4.6 Simulated primary voltage, $v_p$ for $V_i = 40V$ . . . . .	89
4.7 Experimental primary voltage, $v_p$ for $V_i = 40V$ . . . . .	89
4.8 Simulated $v_{ls}$ for $V_i = 40V$ . . . . .	90

4.9	Experimental $v_{ts}$ for $V_i = 40V$ . . . . .	90
4.10	Simulated $v_{cs}$ for $V_i = 40V$ . . . . .	91
4.11	Experimental $v_{cs}$ for $V_i = 40V$ . . . . .	91
4.12	Simulated phase shift modulated input voltage, $v_s$ , for $V_i = 60V$ , $\delta = 114^\circ$ . . . . .	92
4.13	Experimental PSM input voltage, $v_s$ , for $V_i = 60V$ . . . . .	92
4.14	Simulated primary voltage, $v_p$ for $V_i = 60V$ . . . . .	93
4.15	Experimental primary voltage, $v_p$ for $V_i = 60V$ . . . . .	93
4.16	Simulated $v_{ts}$ for $V_i = 60V$ . . . . .	94
4.17	Experimental $v_{ts}$ for $V_i = 60V$ . . . . .	94
4.18	Simulated $v_{cs}$ for $V_i = 60V$ . . . . .	95
4.19	Experimental $v_{cs}$ for $V_i = 60V$ . . . . .	95
4.20	Experimental drain to source voltage $v_{ds}$ for $V_i = 40V$ . . . . .	96
4.21	Experimental voltage across the diode rectifier , $v_{dr}$ for $V_i = 40V$ . . . . .	96
4.22	Experimental current in the secondary winding, $i_p'$ for $V_i = 40V$ . . . . .	97
4.23	Experimental drain to source voltage $v_{ds}$ for $V_i = 60V$ . . . . .	97
4.24	Experimental voltage across the diode rectifier, $v_{dr}$ for $V_i = 60V$ . . . . .	98
4.25	Experimental current in the secondary winding, $i_p'$ for $V_i = 60V$ . . . . .	98
4.26	Converter efficiency with load, $V_i = 40V$ . . . . .	100
4.27	Simulated phase shift modulated input voltage, $v_s$ , for $V_i = 40V$ . . . . .	101
4.28	Experimental PSM input voltage, $v_s$ , for $V_i = 40V$ . . . . .	101
4.29	Simulated primary voltage, $v_p$ for $V_i = 40V$ . . . . .	102
4.30	Experimental primary voltage, $v_p$ for $V_i = 40V$ . . . . .	102
4.31	Simulated resonant current, $i_s$ , for $V_i = 40V$ . . . . .	103
4.32	Experimental resonant current, $i_s$ , for $V_i = 40V$ . . . . .	103
4.33	Simulated phase shift modulated input voltage, $v_s$ , for $V_i = 60V$ . . . . .	104

4.34	Experimental PSM input voltage, $v_s$ for $V_i = 60V$ . . . . .	104
4.35	Simulated primary voltage, $v_p$ for $V_i = 60V$ . . . . .	105
4.36	Experimental primary voltage, $v_p$ for $V_i = 60V$ . . . . .	105
4.37	Simulated resonant current, $i_s$ for $V_i = 60V$ . . . . .	106
4.38	Experimental resonant current, $i_s$ for $V_i = 60V$ . . . . .	106
4.39	Experimental drain to source voltage across one power switch, $v_{ds}$ for $V_i = 40V$ . . . . .	107
4.40	Experimental voltage across the diode rectifier, $v_{dr}$ for $V_i = 40V$ . . .	107
4.41	Experimental voltage across the tertiary winding, $v_t$ for $V_i = 40V$ . .	108
4.42	Experimental drain to source voltage across one power switch, $v_{ds}$ for $V_i = 60V$ . . . . .	108
4.43	Experimental voltage across the tertiary winding, $v_t$ for $V_i = 60V$ . .	109

## List of Tables

4.1	Experimental results showing efficiency with variation in load for $V_i = 40V$ . . . . .	86
4.2	Experimental results showing efficiency with variation in load for $V_i = 60V$ . . . . .	86
4.3	Experimental results showing the variation in efficiency with load for $V_i = 40V$ , for tertiary side resonance . . . . .	99

# Chapter 1

## Introduction

Converters are basic power electronics circuits used to efficiently alter the characteristics of electrical energy. They provide an interface between two power systems which are external to them and thereby impose relationships between the voltage and current waveforms at one port and those at the other. Converters can perform transformation from ac to dc, dc to ac, dc to dc and ac to ac. Dc/dc converters alter the amplitude of input waveforms, while, ac/ac converters can alter phase and frequency along with amplitude.

Ac/dc converters are present in every piece of line-operated electronic equipment - from table radios to computers. They also are used extensively in industrial controls and processes, such as variable speed motor drives, induction heating, plating, and the electrolytic production of chemicals.

Dc/dc converters are used extensively in power supplies for electronic equipment. They take the output of the ac/dc converter and transform it to the different dc voltages required by the particular application, for example,  $\pm 5V$  and  $\pm 12V$ . Dc/dc converters are also used in battery powered equipment and to control the speed of dc motors in many traction applications.

Dc/dc converters can be classified into two categories, depending on the method

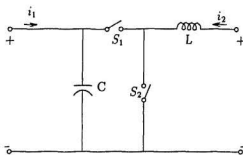


Figure 1.1: Simplified pulse-width modulated dc/dc converter topology

of dc to ac conversion:

- Pulse Width Modulated (PWM) dc/dc converters
- Resonant dc/dc converters

A brief review of the operation, features, analysis methods and control of the two types of dc/dc converters are described below.

## 1.1 PWM dc/dc converters

Figure 1.1 shows a simplified pulse-width modulated dc/dc converter topology. The two switches operate at a constant switching frequency and are controlled so as to be complementary. That is, when one is closed, the other is open. The input current contains substantial ripple caused by switching. Although the output current is ripple-free, the output voltage is not. To obtain a desired ripple-free input current and output voltage, a low-pass filter consisting of a large capacitor,  $C$ , at the input and a large inductor,  $L$ , at the output, is inserted. There are many different PWM converters, i.e., Buck, Boost, Buck/Boost and Ćuk. These converters have been described extensively in the literature [1]-[4]. Landsman [1] describes the similarities

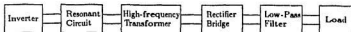


Figure 1.2: Block diagram of a dc/dc resonant converter

among various dc/dc converter topologies and Severns [2] covers all the variations in PWM dc/dc converter topologies in details. A more concise and mathematical treatment of dc/dc converters can be found in [3], and the Ćuk converter is first presented by Middelbrook et al. [4].

In all PWM converters, the controlled switches are required to turn-on and turn-off the entire load current during each switching. This results in high switching stresses and high switching power losses. This also produces electromagnetic interference due to the large  $dv/dt$  and  $di/dt$ .

## 1.2 Resonant dc/dc converters

In resonant converters, first, the switches of the inverter create a square-wave ac waveform from the dc source. A resonant LC circuit tuned to the switching frequency is then used to remove harmonics from the square-wave ac waveform. Hence the name *resonant converter*. This LC circuit can be made very selective by keeping its quality factor  $Q$  high [5]. The filtered, nearly sinusoidal waveform, is rectified to get a dc output. The rectified waveform is then filtered through a low-pass filter to give a ripple-free dc at the output. Figure 1.2 shows the block diagram of a basic resonant converter with a high-frequency isolation transformer.

In resonant converters, the semiconductor devices can be made to switch on and

switch off at either zero current or zero voltage, thereby significantly reducing the switching losses [5]. The reduced dissipation allows these converters to be operated at higher switching frequencies than is possible in case of PWM converters. Unfortunately, in return for the lower switching losses, the switches are subjected to higher on-state currents and off-state voltages, resulting in higher component stresses and higher conduction losses than they would have in PWM converters operating at the same power level. Therefore, more expensive devices are often required.

Resonant converters can be broadly classified into three categories depending on how the load is connected to the LC resonant circuit, i.e., series, parallel and series-parallel (combination of the previous two).

### 1.2.1 Series resonant converters

Figure 1.3 shows the basic configuration of a Series Resonant Converter (SRC). A square-wave output from an inverter is applied to the series resonant LC network, normally tuned to the switching frequency of the inverter, to generate an oscillating current in the resonant circuit. This current when rectified and filtered results in the dc output voltage. A high-frequency transformer provides isolation and transformation. The magnitude of the output voltage is determined by the magnitude and wave-shape of the oscillating or resonant current, and by the load resistance. The resonant current and hence the output voltage, depends on the frequency at which the LC network is excited. A series resonant converter operates in either a Continuous Conduction Mode (CCM) or Discontinuous Conduction Mode (DCM) depending on the load resistance and switching frequency.

SRCs, due to their small size and high efficiency, are extensively used in aerospace industry. Many researchers have carried out extensive research in modeling and anal-

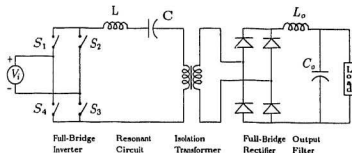


Figure 1.3: Basic circuit of a series resonant converter

ysis of these converters. Accurate steady-state analysis for half-bridge and full-bridge SRCs are presented in [6] and [7]. The analysis, though complete, is difficult to apply to design problems because of the use of the diode conduction angle as a design parameter. Vorperian and Čuk [8] provide a complete solution for the dc conversion ratio of the series resonant converter with an assumption of constant load. The solution requires iterative computation for dc conversion ratio and a new solution is required for any change in circuit parameter.

An output plane model, in which the output current is plotted versus output voltage for constant switching frequency, is developed by Witulski *et al.* [9]. These plots provide convenient reference for designers. Oruganti, *et al.* [10] employ a graphical representation of the state-plane analysis to study the performance of SRCs. This method gives a good insight into the converter operation, but provides little quantitative information required for the converter design. Lee *et al.* [11] apply a similar state-plane approach for quantitative analysis and design of the converter. A similar state-plane analysis is also performed on a constant frequency SRC by Tsai *et al.* [12].

Fourier series analysis [13] provides a simple generalized method for the analysis

of resonant converters. This simple model can be used to analyze many converter topologies. The design curves for the resonant circuit design are also presented in [13]. Small signal equivalent circuit models provide useful information about converter dynamics in an accessible, flexible format [14]-[15].

A phase-staggering control method using two or more series resonant power modules in parallel, is suggested by Klaassens [16] as a means of reducing voltage and current ripples at the input and output terminals of a SRC, without increasing the internal pulse frequency and the value of the filter capacitors. The power modules are operated at a constant relative phase-shift. It has been shown that the output ripple decreases with increasing number of modules. However, this control method results in significant increase in complexity as well as an increase in the number of switches and resonant circuit components.

The use of frequency variation to control the output voltage, causes many problems. Switching frequency has to be varied over a wide range to accommodate the worst combinations of load and line. Also, the filters and magnetics have to be designed for worst case conditions. These disadvantages of varying the frequency are overcome by fixing the switching frequency and using pulse width modulation to control the output voltage [12], [17], [18]. Constant-frequency operation allows the design of filters and magnetic components to be optimized at a specific frequency which improves the efficiency of these components.

A combination of PWM and current-controlled switching strategy is suggested by Ngo [17] for efficient operation during wide range of load variation. A detailed comparison of different modes of operation of fixed-frequency SRC is given in [18]. It is shown that the discontinuous mode of operation causes higher switching losses and should therefore be avoided.

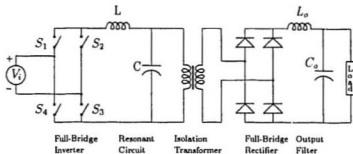


Figure 1.4: Basic configuration of a parallel resonant converter with isolation transformer

Series resonant converters are not very attractive for low voltage, high current applications because the output filter capacitor carries high ripple currents [19].

### 1.2.2 Parallel resonant converters

Figure 1.4 shows the basic configuration of a Parallel Resonant Converter (PRC). In PRCs the load is connected in parallel to the capacitor of the resonant circuit. A square-wave from the inverter is applied to the parallel resonant circuit which produces an oscillating voltage across the parallel capacitor. This oscillating voltage, when rectified and filtered, produces the dc output voltage. The main advantage of this converter over the SRC is that the output dc filter capacitor does not carry high ripple currents. This is because in the PRC, output diodes rectify the voltage and not the current as in the case of SRCs. This characteristic makes this converter desirable for low voltage, high current applications. Another advantage of this converter is that it has a self current limiting capability against an output short circuit [19].

A classical analysis of PRCs with design examples is presented in [20]. PRCs are shown to have good voltage regulation with small variation in operating frequency. State-space approach is used for steady-state analysis of PRC in [21]. Design curves,

for easy selection of circuit components, are also provided. Deb *et al.* [22] describe a frequency-domain analysis which provides simple generalized equations for circuit currents and voltages without going into the considerable computational effort of solving differential equations. In [13], a similar Fourier-series analysis for various resonant converter topologies is presented. Control techniques for resonant converters in general would be studied in the following section.

The main disadvantage of the parallel resonant converter is that the resonant current is independent of load. This leads to low efficiency at light load [23].

### 1.2.3 Series-parallel resonant converter

Series-Parallel Resonant Converter (SPRC), as is evident from its name, is a combination of the above two types and tries to take advantage of the best characteristics of the series and the parallel converter while eliminating their weak points (lack of no-load regulation for the SRC and circulating current independent of load for the PRC). Figure 1.5 shows the basic configuration of a series-parallel resonant converter. The basic SPRC is also called an *LCC* [24]-[25] type resonant converter. As the name suggests, this converter has an *LC* circuit in series and the load is connected in parallel with a second capacitor. A careful selection of the resonant circuit parameters is required for efficient operation of a SPRC. In [23], a simplified analysis of a SPRC is presented and its characteristics are compared with other converter topologies. A more complete analysis, using state-space model, is provided in [24] and [25]. Generalized Fourier-series method of analysis for SPRC is also presented in [13].

Fixed frequency operation of SPRC with pulse-width modulation for voltage regulation is suggested in [26]. A SPRC, with an additional inductor in parallel with the load, is suggested in [27] for low voltage, high current application. A simple

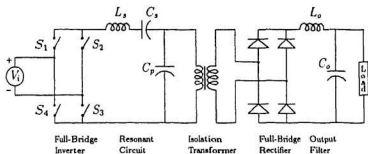


Figure 1.5: Basic series-parallel resonant converter

frequency-domain model is used to analyze this circuit. This circuit is shown to have good efficiency from 10% load to full load. The analysis methods reported in the literature for the SPRC have neglected the effect of the transformer leakage inductance.

A comparison between the three types of converters is presented in [19],[23]. SPRCs have all the advantages over parallel resonant converters, while the only advantage of SPRCs over series resonant converters is the low ripple current rating of the output filter capacitor, therefore, this converter is reserved for low voltage, high current applications [19].

#### 1.2.4 Control methods

Frequency control is the most common method of control to regulate the output voltage of resonant converters [20], [22], [23]. This control method has many disadvantages. For operation during light load conditions, the switching frequency has to be reduced to a very low value. This results in increased size for the magnetic components and the need for lossy  $RC$  snubbers. The converter designed for such low frequency operation when operated at high frequency results in increased magnetic core losses. The design of the control circuit is also quite difficult [26].

There has been a constant effort to overcome the problems associated with frequency control method. Some of the solutions reported are: (1) use of a pulse-width modulated chopper at the input [28], (2) use of phase-shifted resonant inverters [29], (3) use of pulse-width modulation technique [30], (4) use of current-mode control [17], and (5) use of a combination of PWM and current-mode control [17]. Each of the methods eliminates some of the problems associated with frequency control. Fixed-frequency operation with pulse-width modulation for output voltage regulation [19], [26] eliminates all the problems associated with frequency control. By fixing the frequency of operation of the converter, the magnetics can be optimized for that frequency.

### 1.3 Thesis objective

The objective of this thesis is to develop a generalized model for the analysis of a range of resonant converter topologies taking into account the leakage inductance of the high-frequency transformer. A generalized analysis is presented in [13] in which the effect of the leakage reactance has not been considered. Frequency-domain analysis is presented for a series-parallel resonant converter with low voltage, high current output and the effect of leakage inductance of the transformer on the performance of the converter is studied. Simple equations describing the steady-state performance of a range of resonant converters are developed and convenient to use design curves are presented.

Transient analysis of the series-parallel resonant converter is not available in the literature. This analysis is important to study the component stresses in the transient region of operation. Transient analysis is performed using the state-space method.

Series-parallel resonant converter with parallel branch of the resonant circuit on

the tertiary winding of the high-frequency transformer has some advantages over the one with the parallel branch on the primary. Analysis for such a converter is not available in the literature. A frequency-domain model for such a converter is developed and the analysis is performed taking into account the leakage inductance of the transformer. Design curves and a design example using these curves are also presented.

The main objectives of this thesis can be summarized as follows.

1. Development of a generalized model for the analysis of resonant converters, particularly constant frequency PWM series-parallel resonant converter taking into account the leakage inductance of the high-frequency transformer.
2. Transient analysis of the converter to study the transient stresses on the converter components.
3. Development of a model for the analysis of the converter with parallel resonant branch on the tertiary winding of the high-frequency transformer.
4. Development of a model for the analysis of the converter with integrated magnetics.
5. Development of characteristics curves for describing the performance of the various converters.
6. Development of a design procedure for selecting the converter components.
7. Experimental verification of the models and analysis procedures for the different converters.

## 1.4 Thesis outline

This thesis presents the analysis, performance and design of fixed-frequency series-parallel resonant converters with primary and tertiary resonance.

In Chapter 2, the frequency-domain model of the basic fixed-frequency series-parallel resonant converter is presented. An analysis procedure, based on harmonic equivalent circuit is developed and generalized equations are presented. Simulated waveforms as well as the performance and design curves, are also presented. Transient analysis using state-space method and the transient waveforms are presented at the end of the chapter.

In Chapter 3, the frequency-domain model is presented for the converter with tertiary side resonance. Analysis and performance curves as well as simulated waveforms and design curves are presented. The model and analysis of the converter with integrated magnetics is also presented.

In Chapter 4, a design example illustrating the use of design curves for the selection of appropriate component values is presented. Experimental results for the two converters are provided and a comparison is made with simulation results.

A summary of the thesis and recommendations for further work are presented in Chapter 5.

## Chapter 2

# Series-Parallel Resonant Converter With Primary Side Resonance

In this chapter a model for a series-parallel resonant converter is developed, taking into account the leakage inductance of the high frequency transformer. The modeling is done in the frequency domain [31]. Frequency domain modeling provides a simple method for steady-state analysis of the resonant converter. Simple generalized equations are developed. The steady-state performance of the converter is studied and simulation results are presented. Normalized curves showing the effect of the leakage reactance, resonant circuit parameters and load on the converter output voltage are also presented. It is shown that the leakage reactance has a significant effect on the performance of the converter.

Transient analysis of the resonant converter using the state-space method is presented. Simulation results describing the performance of the converter during the transient period are provided.

## 2.1 Circuit description

Figure 2.1 shows the basic series-parallel resonant converter. The converter consists of the following:

**Full-bridge inverter:** The inverter consists of four MOSFETs,  $S_1$  to  $S_4$ , which are used for high-speed switching.  $D_1$  to  $D_4$  represent the body diodes of the MOSFETs. The inverter converts the dc voltage,  $V_i$ , to a high frequency quasi-square waveform by employing a constant frequency, Phase-Shift Modulation (PSM) control technique. This quasi-square waveform,  $v_s$ , is fed into the resonant circuit which is the next stage of the converter. The capacitors,  $C_1$  to  $C_4$ , are snubber capacitors, used to reduce the switching stresses.

**Resonant Circuit:** The resonant circuit consists of a series branch and a parallel branch. The series branch is made up of an inductor,  $L_s$ , and a capacitor,  $C_s$ . Similarly the parallel branch consists of an inductor,  $L_p$ , and a capacitor,  $C_p$ . The two branches can either be tuned or off-tuned depending on the application. Different resonant circuit topologies can be achieved by removing one or more of the resonant components. The resonant circuit shapes the quasi-square waveform to produce a near-sinusoidal voltage,  $v_p$ , across the parallel branch.

**Output Transformer:** The high-frequency transformer provides isolation as well as the transformation of the primary voltage,  $v_p$ , to the required output voltage.

**Diode Rectifier:** The diode rectifier converts the high-frequency near-sinusoidal voltage to a unidirectional output voltage,  $v_r$ , which is filtered to get a ripple-free output voltage.

**Output Filter:** This filter consists of an inductor,  $L_o$ , and a capacitor,  $C_o$ . The inductor provides almost constant output current,  $I_o$ , and the capacitor gives a

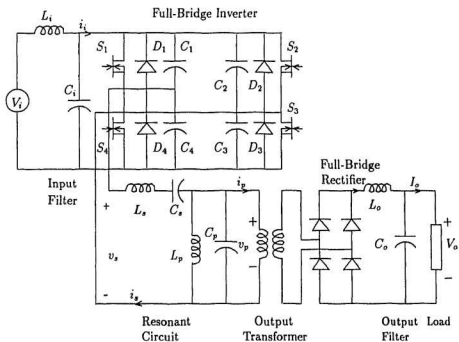


Figure 2.1: Circuit diagram of the dc/dc resonant converter

ripple-free output voltage,  $V_o$ .

## 2.2 Frequency-domain model

Frequency-domain model, as described in [22], is used to perform the steady-state analysis of the converter because of its simplicity and adaptability to a whole range of resonant circuit topologies. Frequency-domain analysis results in simple equations which are easy to manipulate in order to study the effect of variation in circuit parameters on the performance of the converter. Figure 2.2 shows the simplified circuit of the series-parallel resonant converter. The output of the resonant circuit is mod-

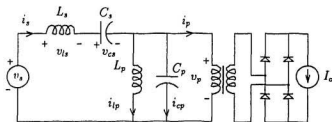


Figure 2.2: Simplified circuit of the dc/dc resonant converter

elled as a current source,  $I_o$ . Due to the presence of the leakage inductance,  $X_l$ , of the transformer the current,  $i_p$ , cannot change direction instantaneously. There is a brief commutation period during which the rectifier diodes are conducting simultaneously causing a short-circuit across the parallel capacitor,  $C_p$ . Therefore, the current through the primary of the transformer,  $i_p$ , is assumed to be trapezoidal.

Figure 2.3 shows the  $n$ th harmonic equivalent circuit of the converter. The voltage,  $v_{sn}$ , is the  $n$ th harmonic component of the PSM input voltage,  $v_s$ , and  $i_{pn}$  is the  $n$ th harmonic component of  $i_p$ . This model is used to study the steady-state performance of the converter. However, the model can also be used to analyze any resonant converter topology by shorting or opening the appropriate series or parallel branch of the resonant circuit. In addition, the model allows the performance of the converter to be studied for various operating conditions such as, series and parallel elements tuned above or below the operating frequency.

### 2.3 Steady-state analysis of the converter

In this section, the steady-state analysis of the series-parallel converter, using the frequency-domain model, is presented. Generalized equations based on Fourier analysis are developed, and a procedure for obtaining the steady-state performance of the

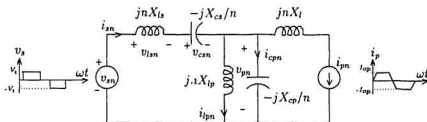


Figure 2.3:  $n$ th harmonic equivalent circuit of the converter

converter is described.

### 2.3.1 Assumptions

The following simplifying assumptions are used.

1. All the switches are ideal i.e. they provide zero resistance when they are turned on and infinite resistance when they are off and the transition from one state to another is instantaneous.
2. The input filter inductor,  $L_i$ , is big enough to provide a ripple-free input current,  $I_i$ , and the output filter capacitor,  $C_o$ , provides a ripple-free output voltage,  $V_o$ , to the load.
3. The current,  $i_p$ , varies linearly between  $-I_{op}$  and  $+I_{op}$ , during the commutation interval,  $\mu$ , and is therefore assumed to be trapezoidal.
4. The high-frequency isolation transformer has a unity turns-ratio. Also the transformer is assumed to be ideal except for its leakage inductance.

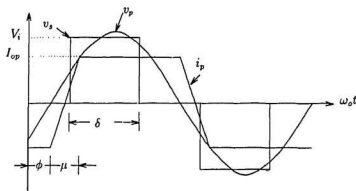


Figure 2.4: Generalized waveforms of the dc/dc resonant converter

### 2.3.2 Frequency-domain analysis

Figure 2.4 shows the generalized steady-state waveforms of the input voltage,  $v_s$ , output voltage,  $v_p$ , and the output current,  $i_p$ . The angle,  $\phi$ , is the phase difference between the fundamental component of the PWM voltage,  $v_s$ , and the transformer primary voltage,  $v_p$ . The pulse-width of the voltage,  $v_s$ , and the commutation interval are specified by the angles  $\delta$  and  $\mu$  respectively.

The Fourier representation of the  $n$ th harmonic component of  $v_s$ , can be written as

$$v_{sn} = \frac{4V_i}{n\pi} \sin\left(\frac{n\pi}{2}\right) \sin\left(\frac{n\delta}{2}\right) \sin(n\omega_0 t), \quad (2.1)$$

and the  $n$ th harmonic component of  $i_p$  is

$$i_{pn} = \frac{8I_{op}}{\pi\mu n^2} \sin\left(\frac{n\mu}{2}\right) \sin\left[n\left(\omega t - \phi - \frac{\mu}{2}\right)\right], \quad (2.2)$$

where  $I_{op}$  is the output current referred to the primary.

Using the superposition theorem the  $n$ th harmonic current  $i_{sn}$  in the circuit of fig. 2.3 is obtained as

$$i_{sn} = \frac{4V_i}{n\pi Z_{in}} \sin\left(\frac{n\pi}{2}\right) \cos(n\omega_o t) + \dots \\ + \frac{8I_{op}}{\pi\mu n^2} \sin\left(\frac{n\mu}{2}\right) \sin\left[n\left(\omega_o t - \phi - \frac{\mu}{2}\right)\right] \frac{Z_{pn}}{Z_{in}}. \quad (2.3)$$

Similarly, the  $n$ th harmonic voltage  $v_{pn}$  is obtained as

$$v_{pn} = \frac{4V_i Z_{pn}}{n\pi Z_{in}} \sin\left(\frac{n\pi}{2}\right) \sin\left(\frac{n\delta}{2}\right) \sin(n\omega_o t) + \dots \\ + \frac{8I_{op}}{\pi\mu n^2} \sin\left(\frac{n\mu}{2}\right) \cos\left[n\left(\omega_o t - \phi - \frac{\mu}{2}\right)\right] \frac{Z_{pn} Z_{sn}}{Z_{in}}, \quad (2.4)$$

where

$$Z_{sn} = j\left(nX_{Ls} - \frac{X_{Cs}}{n}\right) \quad (2.5)$$

$$Z_{pn} = -j\frac{X_{Lp}X_{Cp}}{nX_{Lp} - \frac{X_{Cs}}{n}} \quad (2.6)$$

$$Z_{in} = Z_{sn} + Z_{pn} \quad (2.7)$$

The input voltage,  $v_s$ , the resonant current,  $i_s$ , the transformer primary current,  $i_p$ , and the parallel voltage,  $v_p$ , are expressed as the sum of  $n$  odd harmonics i.e.,

$$v_s = \sum_{n=1,3,\dots}^{\infty} v_{sn} \quad (2.8)$$

$$i_s = \sum_{n=1,3,\dots}^{\infty} i_{sn} \quad (2.9)$$

$$v_p = \sum_{n=1,3,\dots}^{\infty} v_{pn} \quad (2.10)$$

$$i_p = \sum_{n=1,3,\dots}^{\infty} i_{pn} \quad (2.11)$$

### 2.3.3 Normalization

In order to obtain general equations that are independent of the absolute values of the resonant parameters and output voltage, Equations 2.1 to 2.5 are normalized.

The three base quantities are chosen to be:

$$\text{Base Voltage} = V_i$$

$$\text{Base Reactance} = R_l$$

$$\text{Base Frequency} = f_s$$

where  $V_i$  is the dc input voltage to the inverter,  $R_l$  is the load resistance and  $f_s$  is the switching frequency.

The normalized expressions for the  $n$ th harmonic components of the circuit variables can be written as:

$$v_{snN} = \frac{4}{n\pi} \sin\left(\frac{n\pi}{2}\right) \sin\left(\frac{n\delta}{2}\right) \sin(n\omega_o t) \quad (2.12)$$

$$i_{pnN} = \frac{8I_{opN}}{\pi\mu n^2} \sin\left(\frac{n\mu}{2}\right) \sin\left[n\left(\omega t - \phi - \frac{\mu}{2}\right)\right] \quad (2.13)$$

$$i_{snN} = \frac{4}{n\pi Z_{in}} \sin\left(\frac{n\pi}{2}\right) \cos(n\omega_o t) + \dots \\ + \frac{8I_{opN}}{\pi\mu n^2} \sin\left(\frac{n\mu}{2}\right) \sin\left[n\left(\omega_o t - \phi - \frac{\mu}{2}\right)\right] \frac{Z_{pnN}}{Z_{inN}} \quad (2.14)$$

$$v_{pnN} = \frac{4Z_{pnN}}{n\pi Z_{inN}} \sin\left(\frac{n\pi}{2}\right) \sin\left(\frac{n\delta}{2}\right) \sin(n\omega_o t) + \dots \\ + \frac{8I_{opN}}{\pi\mu n^2} \sin\left(\frac{n\mu}{2}\right) \cos\left[n\left(\omega_o t - \phi - \frac{\mu}{2}\right)\right] \frac{Z_{pnN}Z_{snN}}{Z_{inN}} \quad (2.15)$$

Equations for other parameters such as  $v_{csnN}$ ,  $v_{IsnN}$ ,  $i_{lpnN}$  and  $i_{cpnN}$  can also be written as follows.

$$v_{csnN} = -\frac{4X_{cs}}{n^2\pi Z_{inN}} \sin\left(\frac{n\pi}{2}\right) \sin\left(\frac{n\delta}{2}\right) \sin(n\omega_o t) - \dots \\ \frac{8I_{opN}}{\pi\mu n^3} \sin\left(\frac{n\mu}{2}\right) \cos\left[n\left(\omega_o t - \phi - \frac{\mu}{2}\right)\right] \frac{X_{cs}Z_{pnN}}{Z_{inN}} \quad (2.16)$$

$$i_{lpnN} = -\frac{4Z_{pnN}}{n^2\pi X_{lp}Z_{inN}} \sin\left(\frac{n\pi}{2}\right) \sin\left(\frac{n\delta}{2}\right) \cos(n\omega_o t) + \dots \\ + \frac{8I_{opN}}{\pi\mu n^3} \sin\left(\frac{n\mu}{2}\right) \sin\left[n\left(\omega_o t - \phi - \frac{\mu}{2}\right)\right] \frac{Z_{pnN}Z_{snN}}{X_{lp}Z_{inN}} \quad (2.17)$$

Knowing  $v_{csnN}$  and  $i_{lpnN}$ , the variables  $v_{IsnN}$  and  $i_{cpnN}$  are obtained as follows.

$$v_{IsnN} = v_{snN} - v_{pnN} - v_{csnN} \quad (2.18)$$

$$i_{cpnN} = i_{snN} - i_{pnN} - i_{lpnN} \quad (2.19)$$

Equations 2.12 to 2.19 are the generalized equations which can be used to describe the steady-state performance of the converter. However, the parameters  $\phi$ ,  $\mu$ , and  $I_{opN}$  need to be determined. The procedure adopted is described in the next section.

### 2.3.4 Solution of equations

Three equations are required to obtain a unique solution for  $\phi$ ,  $\mu$  and  $I_{opN}$ . The first equation is obtained from the condition that  $v_p = 0$  at  $\omega_o t = \phi$ . From Equation 2.15 the following equation is obtained.

$$\sum_{n=1,3,\dots}^{\infty} \frac{4}{n\pi} \sin\left(\frac{n\pi}{2}\right) \sin\left(\frac{n\delta}{2}\right) \sin(n\phi) \frac{Z_{pn}}{Z_{in}} + \dots \\ + \sum_{n=1,3,\dots}^{\infty} \frac{8I_{opN}}{\pi\mu n^2} \sin\left(\frac{n\mu}{2}\right) \cos\left(\frac{n\mu}{2}\right) \frac{Z_{pn}Z_{sn}}{Z_{in}} = 0 \quad (2.20)$$

The second equation is obtained from the condition that the normalized output voltage  $V_{opN}$ , referred to the primary is equal to the normalized primary current,  $I_{opN}$ , and can be written as the average of  $v_p$  over the interval  $\phi + \mu/2$  to  $\phi + \pi$ . From equation 2.15 the following equation is obtained.

$$V_{opN} = \frac{1}{\pi} \int_{\phi+\mu/2}^{\phi+\pi} v_p d\omega t \\ = \sum_{n=1,3,\dots}^{\infty} \frac{4}{\pi^2 n^2} \sin\left(\frac{n\pi}{2}\right) \sin\left(\frac{n\delta}{2}\right) \frac{Z_{pn}}{Z_{in}} \dots \\ \cdot [\cos(n(\phi + \mu)) + \cos(n\phi)]. \quad (2.21)$$

The third equation is obtained by assuming that the primary voltage,  $v_p$ , is sinusoidal. During the commutation interval,  $\mu$ , the equivalent circuit of the output is shown in Fig. 2.5. Using this equivalent circuit an approximate normalized expression for the commutation angle,  $\mu$ , can be obtained. From Fig. 2.5(b) the following

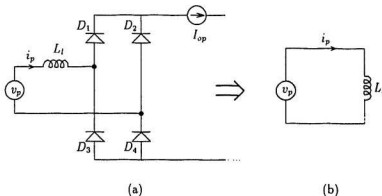


Figure 2.5: Equivalent circuit during the commutation period,  $\mu$

differential equation can be obtained.

$$\frac{di_p}{d(\omega_0 t)} = \frac{v_p}{X_l}, \quad \text{for } \phi \leq \omega_0 t \leq \phi + \mu \quad (2.22)$$

It is assumed that  $v_p$  is sinusoidal, i.e.,

$$v_p = V_{pmax} \sin(\omega_0 t) \quad (2.23)$$

Now, taking the integral of Equation 2.27 gives,

$$\begin{aligned} i_p &= \frac{1}{X_l} \int V_{pNmax} \sin(\omega_0 t) d(\omega_0 t) \\ &= \frac{1}{X_l} [-V_{pNmax} \cos(\omega_0 t)] + K \end{aligned} \quad (2.24)$$

where  $K$  is a constant of integration.

At  $\omega_0 t = 0$ ,  $i_p = -I_{opN}$  and at  $\omega_0 t = \mu$ ,  $i_p = +I_{opN}$ . Substituting these two conditions in Equation 2.24 gives:

$$-I_{opN} = \frac{1}{X_l} [-V_{pNmax} \cos(0)] + K \quad (2.25)$$

$$+ I_{opN} = \frac{1}{X_l} [-V_{pNmax} \cos(\mu)] + K \quad (2.26)$$

Subtracting equation 2.25 from Equation 2.26 gives

$$2I_{opN}X_l = V_{pNmax} [1 - \cos(\mu)] \quad (2.27)$$

The commutation angle,  $\mu$ , is obtained from Equation 2.27 as

$$\cos(\mu) = 1 - \frac{2X_l I_{opN}}{V_{pNmax}}. \quad (2.28)$$

Equations (2.20), (2.21) and (2.28) are in four unknowns  $\phi$ ,  $\mu$ ,  $I_{opN}$  and  $V_{pNmax}$ . Therefore, an iterative method is used to obtain these parameters. The procedure is as follows.

1. Values of normalized resonant circuit parameters, transformer leakage reactance and  $\delta$ , are specified.
2. An initial value of  $\mu$  is arbitrarily selected.
3. Equations (2.20) and (2.21) are solved for  $\phi$  and  $V_{opN}(= I_{opN})$ .
4. Equation (2.15) is then used to determine  $V_{pNmax}$ .
5. Equation (2.28) is used to calculate a new value of  $\mu$ .
6. With a new value of  $\mu$ , steps 2 to 5 are repeated until  $\mu$  converges.

After finding the values of  $\phi$ ,  $\mu$  and  $I_{opN}$ , Equations (2.12) to (2.19) are solved to obtain the various circuit waveforms. These waveforms are then used to describe the performance of the converter. The generalized equations are also employed to investigate the effect of various circuit parameters on the performance of the converter.

## 2.4 Steady-state performance

The method described in the previous section, is used to obtain the waveforms for the various converter parameters. The resonant component ratios are varied to study the performance of the converter for different modes of operation. As all the parameters are normalized, a dimensionless parameter  $K$  is chosen to describe the variations in the resonant components. The parameter  $K$  is specified as follows:

1. The series resonant components, described by the ratio,  $K_s$ , defined as the ratio of the series capacitive reactance,  $X_{cs}$ , to the series inductive reactance,  $X_{ls}$ , (i.e.  $K_s = X_{cs}/X_{ls}$ ). The effect of the series components on the performance of the converter is studied by varying  $K_s$  so as to make the series resonant circuit inductive,  $K_s < 1$  (for example,  $K_s = 0.6$ ), resonant (i.e.,  $K_s = 1$ ) and capacitive,  $K_s > 1$  (for example,  $K_s = 1.4$ ).
2. The parallel resonant components, described by the ratio,  $K_p$ , defined as the ratio of the parallel capacitive reactance,  $X_{cp}$ , to the parallel inductive reactance,  $X_{lp}$  (i.e.,  $K_p = X_{cp}/X_{lp}$ ). Similarly,  $K_p$  is varied so as to make the parallel resonant circuit inductive,  $K_p < 1$  (for example,  $K_p = 0.5$ ), near resonance (i.e.,  $K_p \approx 1$ ) and capacitive  $K_p > 1$  (for example,  $K_p = 2$ ).
3.  $K_I$  is described as the ratio of the series inductive reactance,  $X_{ls}$ , to the parallel inductive reactance,  $X_{lp}$  (i.e.,  $K_I = X_{ls}/X_{lp}$ ).  $K_I$  is varied from 2 to 6.

In the discussion which follows, the fundamental components of the input voltage is taken to be the point of reference for all angles i.e., it is at zero phase.

### 2.4.1 Simulated waveforms

Figures 2.6 to 2.12 show the waveforms for the input PWM voltage,  $v_s$ , the resonant current,  $i_s$ , the voltage across the primary of the transformer,  $v_p$ , and the current through it,  $i_p$ , for different values of  $K_s$  and  $K_p$ . Various converter parameters are listed on the upper right hand corner of the plot.

Figures 2.6 and 2.7 show that  $v_s$ ,  $i_s$  and  $i_p$  are almost identical but the voltage  $v_p$  is closer to sinusoidal in Fig. 2.7 ( $K_l = 4$ ) than in Fig. 2.6 ( $K_l = 2$ ). It is noted that the higher the ratio of  $X_{ls}$  to  $X_{lp}$  the more sinusoidal the voltage waveform  $v_p$  becomes. In both figures, the series branch is tuned and the parallel branch is as closely tuned as possible (i.e.  $K_p = 1.0001$  since putting  $K_p = 1$  makes the parallel branch reactance,  $X_p = \infty$ ). As the series branch is tuned the angle  $\phi$  is zero.

Figure 2.8 shows the waveforms when the parallel resonant branch is inductive and the series branch is tuned. The voltage waveform,  $v_p$ , remains almost the same but the resonant current,  $i_s$ , is higher and also leads the voltage,  $v_p$ . This is not desirable as the higher values of  $i_s$  result in higher losses and therefore lower efficiency.

Figure 2.9 shows the waveforms when the parallel branch is capacitive and the series branch is tuned. The voltage,  $v_p$ , in this case is much more distorted and the resonant current,  $i_s$ , is higher. The higher distortion in  $v_p$  requires larger output filter to reduce the output ripple.

Figure 2.10 shows waveforms when the series branch is inductive and the parallel branch is nearly tuned. In this case the voltage  $v_p$  lags behind the fundamental component of input voltage  $v_s$ . The voltage waveform,  $v_p$ , is quite distorted. The resonant current is almost at zero phase and it is also higher than that of a tuned series resonant circuit. In Fig. 2.11 the series resonant circuit is capacitive. Both the resonant current,  $i_s$ , and the voltage,  $v_p$ , are lagging. In this case, the current is quite

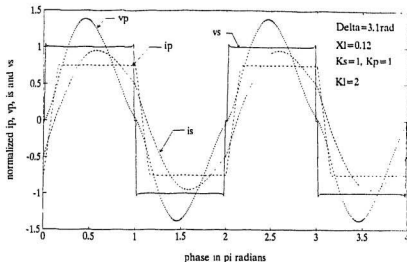


Figure 2.6: Simulated waveforms of the converter for tuned series and parallel branches

low and the voltage waveform is also quite close to sinusoidal.

Figure 2.12 shows the simulated waveforms for  $\delta = 92^\circ$ . This represents the case when high inverter input voltage is to be matched to a specified output voltage. A smaller value of  $\delta$  is required to achieve this goal. It can be seen that this condition results in a distorted primary voltage,  $v_p$ , but as the resonant current,  $i_s$ , is lagging the switching losses are low.

#### 2.4.2 Effect of various parameters on the output voltage of the converter

In this section, the steady-state performance of the converter is studied by examining the effect of various converter parameters on the output voltage.

Figure 2.13 shows the effect of the leakage reactance,  $X_l$  on the output voltage,  $V_o$ ,

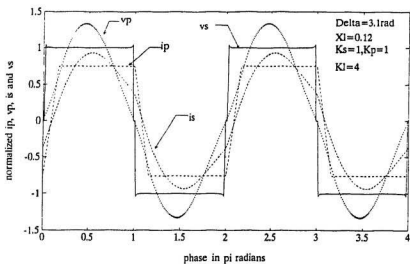


Figure 2.7: Simulated waveforms of the converter with  $K_I = 4$

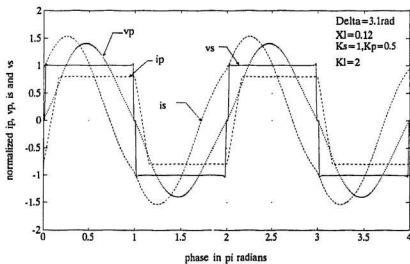


Figure 2.8: Simulated waveforms of the converter for inductive parallel branch

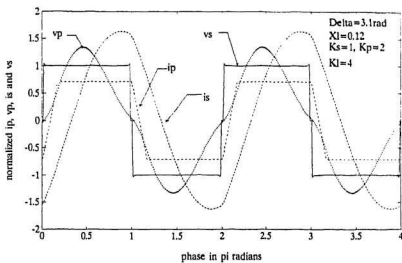


Figure 2.9: Simulated waveforms of the converter for capacitive parallel branch

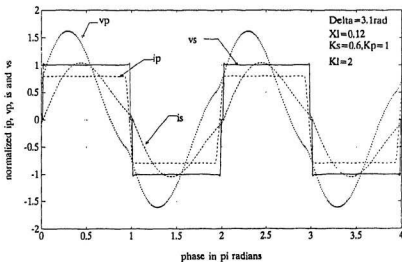


Figure 2.10: Simulated waveforms of the converter for inductive series branch

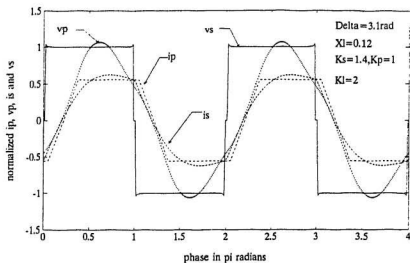


Figure 2.11: Simulated waveforms of the converter for capacitive series branch

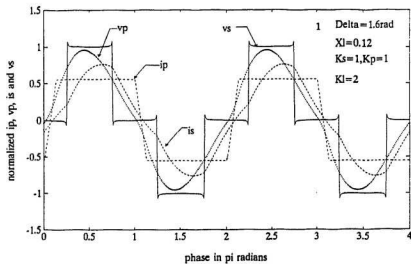


Figure 2.12: Simulated waveforms of the converter for reduced  $\delta$

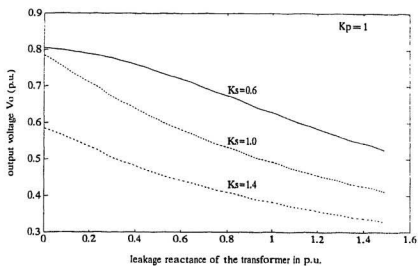


Figure 2.13: Output voltage  $V_o$  vs. leakage reactance for  $K_s = 0.6, 1.0$  and  $1.4$  and  $K_p \approx 1$

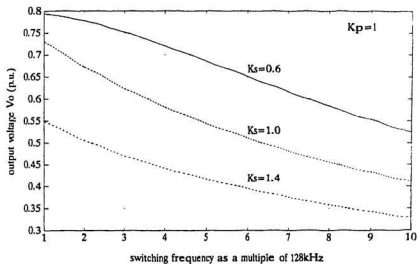


Figure 2.14:  $V_o$  vs. switching frequency  $f_s$  for different values of  $K_s$ , and  $K_p \approx 1$

for three values of  $K_s$ . It can be seen that the output voltage decreases as the leakage reactance increases for all values of  $K_s$ . This drop is significant as  $V_o$  decreases to almost half as the leakage reactance of the transformer increases from 0 to 1.5 p.u. It should also be noted that the output voltage decreases as the series resonant circuit becomes more capacitive. This drop in voltage clearly indicates that the effect of the transformer inductance cannot be ignored while designing the converter.

Figure 2.14 shows the effect of increasing the switching frequency,  $f_s$ , on the output voltage,  $V_o$ . The curve is shown for three values of  $K_s$ . As the switching frequency increases, the output voltage drops significantly. The curves for the three values of  $K_s$ , are almost parallel. The curves show that for higher frequency operation the leakage reactance becomes quite large and therefore the output voltage is significantly reduced.

Figure 2.15 shows the variation of  $V_o$  with  $\delta$  for different values of leakage reactance,  $X_l$ . The effect of  $X_l$  is as expected;  $V_o$  decreases as  $X_l$  increases. The curve shows that for  $\delta < 0.7$  p.u., the variation in the output voltage is almost linear but beyond 0.7 p.u., the output voltage variation with  $\delta$  is quite small. Figure 2.16 shows the same curves for three values of  $K_s$ .

Figure 2.17 shows the effect of output load variation on the output voltage. For these curves, the parallel branch of the resonant circuit is slightly off-tuned i.e.,  $K_p = 1.0001$ . The curves are plotted for three values of  $K_s$ . It can be seen that with tuned series branch (i.e.,  $K_s = 1$ ), the output voltage is independent of load but as the series branch becomes capacitive, the variation in  $V_o$  becomes significant. This suggests that for a fixed output voltage, the series branch of the resonant circuit should be kept tuned. Figure 2.18 shows the same curve for a capacitive parallel branch (i.e.,  $K_p = 2$ ). It can be seen that for  $K_s > 1$ , the output voltage increases

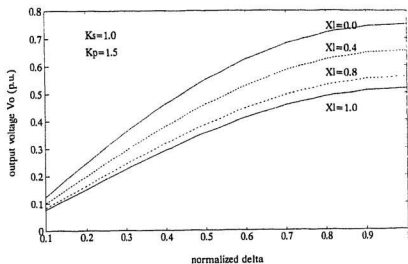


Figure 2.15:  $V_o$  vs.  $\delta$  for different values of  $X_l$ , and  $K_p \approx 1$

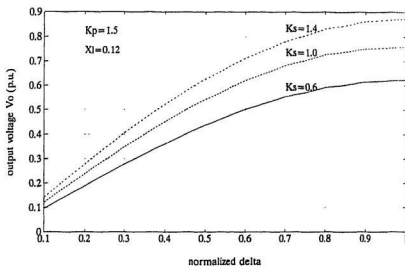


Figure 2.16:  $V_o$  vs.  $\delta$  for different values of  $K_s$ , and  $X_l = 0.12$

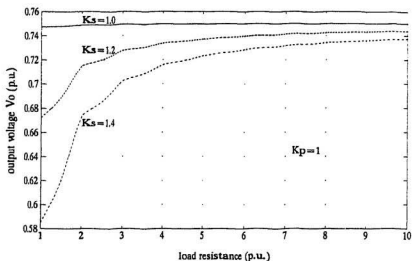


Figure 2.17:  $V_o$  vs. load resistance  $R_l$  for different values of  $K_s$ , and  $K_p \approx 1$

quite significantly with load. When  $K_p = 2$ , the output voltage for  $K_s > 1$ , is higher than that for  $K_s = 1$ . This is because for  $K_p > 1$ , the parallel branch of the resonant circuit is capacitive and therefore, the voltage across it is higher resulting in higher output voltage.

### 2.4.3 $\delta_{min}$ vs. $K_p$

Figure 2.19 shows the variation of the minimum value of  $\delta$  with  $K_p$ , for different values of leakage reactance,  $X_l$ . The minimum value of  $\delta$ ,  $\delta_{min}$ , is the minimum possible value  $\delta$  can have such that the converter remains lossless. For values of  $\delta > \delta_{min}$ ,  $i_s$  lags behind  $v_s$ , which implies that zero voltage switching can be employed to reduce the switching losses. It can be seen from the figure that as  $K_p$  increases, the value of  $\delta_{min}$  decreases resulting in wider range of variation of  $\delta$ . The effect of higher leakage reactance is to increase the range of variation of  $\delta$ .

Figure 2.20 shows the variation of  $\delta_{min}$  with  $K_p$  for four values of the parallel

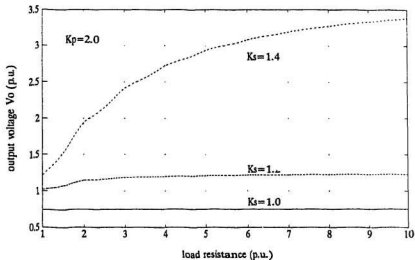


Figure 2.18:  $V_o$  vs. load resistance  $R_l$  for  $K_p = 2$

capacitive reactance,  $X_{cp}$ . It can be seen from this plot that to achieve a wider range of variation in  $\delta$ , the value of  $X_{cp}$  should be kept low.

#### 2.4.4 Resonant current $i_s$ vs. $K_p$

Figure 2.21 shows the variation of resonant current with  $K_p$  for four values of  $X_{cp}$ . The resonant current increases with increasing  $K_p$ . For smaller values of  $X_{cp}$ , the increase is quite significant. Increase in  $i_s$  indicates higher losses and hence lower converter efficiency. For  $K_p$  close to unity, the resonant current is the same for all values of  $X_{cp}$  but if the operation is desired in the range where  $K_p > 1$ , the value of  $X_{cp}$  must be chosen carefully to minimize the losses. It is also seen that for capacitive parallel branch (i.e.,  $K_p > 1$ ), the resonant current rises sharply if the series branch is not tuned. Therefore, for operation with  $K_p > 1$ , the series branch of the resonant circuit should be tuned to the switching frequency and the value of  $X_{cp}$  kept high.

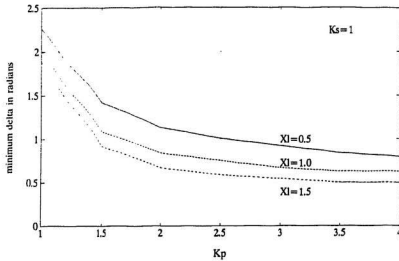


Figure 2.19: Variation of  $\delta_{\min}$  with  $K_p$  for different values of  $\xi_I$ , and  $K_s = 1$

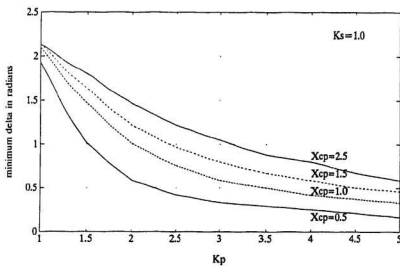


Figure 2.20: Variation of  $\delta_{\min}$  with  $K_p$  for different values of  $X_{cp}$ .

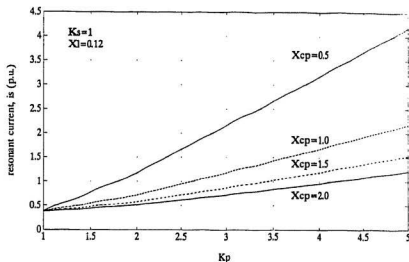


Figure 2.21: Variation of  $i_s$  with  $K_p$  for different values of  $X_{cp}$  and  $K_s = 1$

#### 2.4.5 Inverter input current harmonics vs. $\delta$

Figure 2.22 to 2.26 show the 2nd, 4th and 6th harmonic components of the input current,  $i_{in}$ , for various values of  $K_s$  and  $K_p$ . Figures 2.22 to 2.24 show curves for three values of  $K_s$ . It can be seen that there is very little difference in Fig. 2.22 and 2.24 for an inductive series branch and a tuned series branch ( $K_s = 1.0$  and  $0.6$ ). But for a capacitive series branch (Fig. 2.23) the 2nd harmonic component increases more gradually and does not show a peak as in the other two curves (Fig. 2.22 and 2.24).

Figures 2.25 and 2.26 show the three harmonic components for inductive parallel branch and capacitive parallel branch, respectively. When compared with Fig. 2.22 for a tuned parallel branch it can be noted that the curves are almost identical for inductive parallel branch (Fig. 2.25) and a tuned parallel branch (Fig. 2.22). But for a capacitive parallel branch (Fig. 2.26) the increase in the second harmonic component is more gradual. The value of the second harmonic component is higher in this case

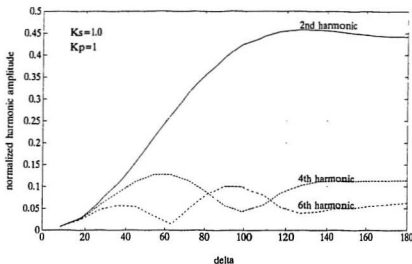


Figure 2.22: Variation of input current harmonics with  $\delta$  for tuned series and parallel branches,  $K_p \approx 1$

as the current for a capacitive parallel branch (i.e.,  $K_p = 2$ ) is higher. These curves are useful for designing the inverter input filter.

#### 2.4.6 Output voltage harmonics vs. commutation angle $\mu$

Figures 2.27 to 2.30 show the variation in the 2nd, 4th and 6th harmonic components of the output voltage with the commutation angle  $\mu$ . It can be seen that the variation in  $K_p$  does not affect the shape of the curves. In general, the 2nd harmonic component increases with increasing leakage reactance. Figures 2.28 and 2.29 show that the harmonics increase for both inductive and capacitive series branches. These curves are required for the selection of output filter components  $L_o$  and  $C_o$ .

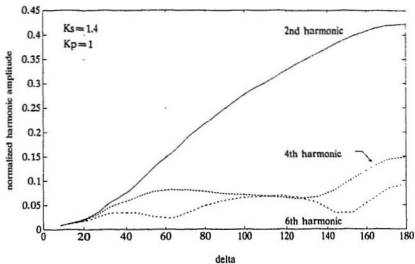


Figure 2.23: Variation of input current harmonics with  $\delta$  for capacitive series branch,  $K_p \approx 1$

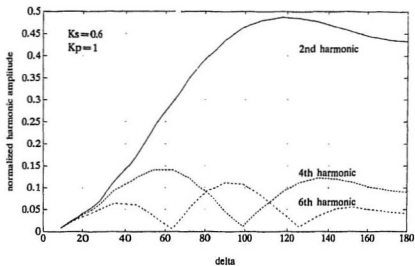


Figure 2.24: Variation of input current harmonics with  $\delta$  for inductive series branch,  $K_p \approx 1$

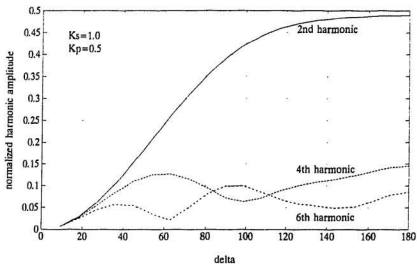


Figure 2.25: Variation of input current harmonics with  $\delta$  for inductive parallel branch,  $K_s = 1$

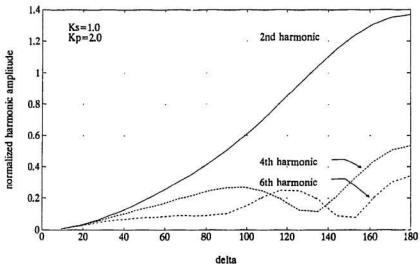


Figure 2.26: Variation of input current harmonics with  $\delta$  for capacitive parallel branch,  $K_s = 1$

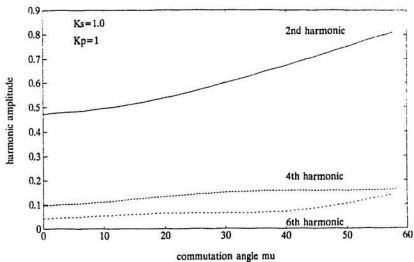


Figure 2.27: Variation of output voltage harmonics with  $\mu$  for tuned series and parallel branches

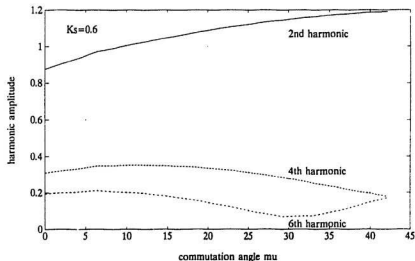


Figure 2.28: Variation of output voltage harmonics with  $\mu$  for inductive series branch

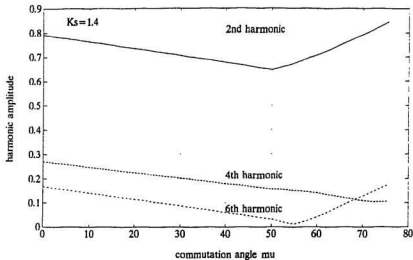


Figure 2.29: Variation of output voltage harmonics with  $\mu$  for capacitive series branch

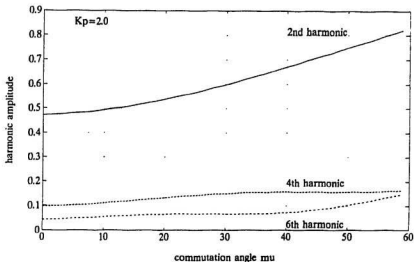


Figure 2.30: Variation of output voltage harmonics with  $\mu$  for capacitive parallel branch

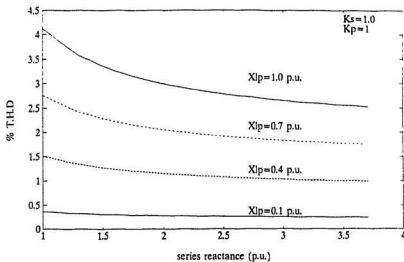


Figure 2.31: Total harmonic distortion with  $X_{lp}$ , and  $K_p \approx 1$

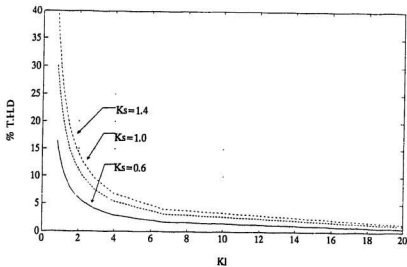


Figure 2.32: Total harmonic distortion with  $K_I$  for capacitive series branch, and  $K_p \approx 1$

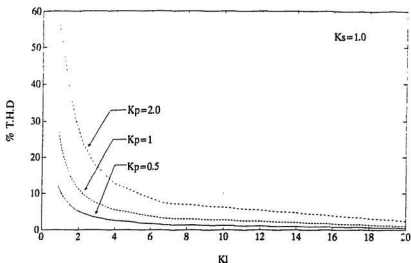


Figure 2.33: Total harmonic distortion with  $K_I$  for tuned series branch

#### 2.4.7 Total harmonic distortion in output voltage

Total Harmonic Distortion (THD) is a measure of distortion in a waveform, and is defined as:

$$\%THD = 100 \times \sqrt{\frac{\sum_{n=2}^{\infty} v_{pn}^2}{v_{p1}^2}} \quad (2.29)$$

where  $v_{pn}$  is the amplitude of the  $n$ th harmonic component of the voltage  $v_p$ . In practical terms, the THD is the square root of the ratio of the power that would be dissipated in a resistor because of the distortion components of a waveform, to the power that would be dissipated because of the fundamental component alone. Figure 2.31 shows the percent total harmonic distortion (%THD) for four values of  $X_{lp}$ , as the series reactance,  $X_{ls}$ , is varied. As  $X_{ls}$  increases, the THD decreases. It can be seen that for  $K_s = 1$  and  $K_p = 1.0001$ , percent THD is below 4% for all values of  $X_{lp}$ .

Figure 2.32 shows the variation in %THD with the ratio  $K_I$  for three values of

$K_s$ . It can be seen that for small values of  $K_t$ , the total harmonic distortion is quite high. Also as the series branch becomes more capacitive the distortion increases. This means that the series reactance must be kept at a value greater than double the value of parallel reactance to keep the %THD low. By properly choosing the resonant circuit components, the %THD can be kept within the required range.

Figure 2.33 shows a similar plot for three values of  $K_p$ . It can be seen from this plot that the THD is higher for higher values of  $K_p$ . In general with the series and parallel branches tuned, the total harmonic distortion of less than 5% can be achieved with  $K_t > 4$ .

## 2.5 Transient analysis

It is important to know the stresses on the various components of the converter. During the transient period of operation, these stresses reach their maximum. The transient analysis of the converter is performed and the currents and voltages associated with the different converter components are studied. The state-space model is used to perform the transient analysis of the converter. This model focuses on the circuit variables (i.e., state variables) which are critical to the transient performance of the converter. In this section the transient analysis of the converter is presented in which the effect of leakage reactance of the high frequency transformer is considered. All the equations presented in this section are normalized.

In addition to the simplifying assumptions stated in section 2.3.1, it is assumed, for the transient analysis, that the initial values of all the circuit variables are zero at  $t = 0$ . As the converter with tuned series branch shows the best performance and also for simplicity, the transient analysis is performed with the series resonant circuit of the series-parallel converter tuned to the switching frequency, i.e.,  $K_s = 1$ .

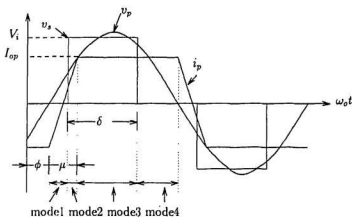


Figure 2.34: Different modes of operation of the converter

### 2.5.1 Analysis

The generalized waveforms for a half-cycle of operation are divided into four modes of operation beginning at the zero-crossing instant of the transformer primary voltage,  $v_p$ . Figure 2.34 shows the four modes of operation of the series-parallel converter. The first mode starts with the zero crossing of the voltage  $v_p$ . This continues till the phase-shift modulated voltage,  $v_s$ , switches from zero to  $V_i$ . The current  $i_p$  at this point is still in the transition mode. Mode 2 starts at the time when the PSM input voltage,  $v_s$ , becomes  $+V_i$  and ends when the current,  $i_p$ , achieves its positive constant value,  $I_{op}$ . This is also the beginning of the third mode of operation. Mode 3 ends when the input voltage,  $v_s$ , goes to zero, and mode 4 starts at this instant. Mode 4 ends with the zero crossing of  $v_p$ .

Figure 2.35(a) to (d) show the equivalent circuits for the four modes. Four sets of differential equations can be written for the four equivalent circuits. For the state-space analysis presented below, the following are chosen as the state variables.

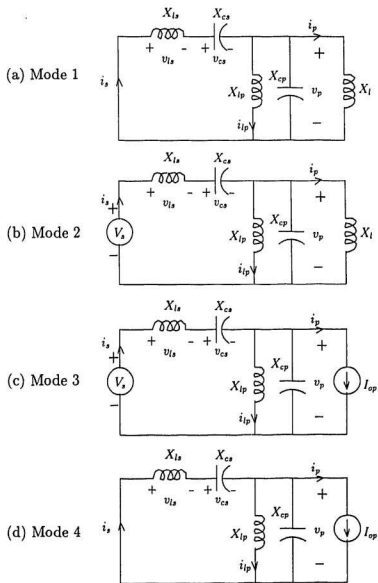


Figure 2.35: Equivalent circuits for the four modes of operations

Resonant current,  $i_s$

Voltage across the transformer primary,  $v_p$

Voltage across the series capacitor,  $v_{cs}$

Current through the parallel inductor,  $i_{lp}$

Current through the transformer primary,  $i_p$ .

From Fig. 2.34, it can be calculated that mode 1 lies between  $\phi$  and  $\frac{\pi-\xi}{2}$ . The differential equations for this mode of operation are obtained as

$$\frac{di_s}{d(\omega_o t)} = -\frac{v_p}{\omega_o L_s} - \frac{v_{cs}}{\omega_o L_s} \quad (2.30)$$

$$\frac{dv_p}{d(\omega_o t)} = \frac{i_s}{\omega_o C_p} - \frac{i_{lp}}{\omega_o C_p} - \frac{i_p}{\omega_o C_p} \quad (2.31)$$

$$\frac{dv_{cs}}{d(\omega_o t)} = \frac{i_s}{\omega_o C_s} \quad (2.32)$$

$$\frac{di_{lp}}{d(\omega_o t)} = \frac{v_p}{\omega_o L_p} \quad (2.33)$$

$$\frac{di_p}{d(\omega_o t)} = \frac{v_p}{\omega_o L_l} \quad (2.34)$$

Mode 2 begins at  $\frac{\pi-\xi}{2}$  and ends at  $\phi + \mu$ , and from Fig. 2.35(b) the following differential equations are obtained.

$$\frac{di_s}{d(\omega_o t)} = \frac{V_i}{\omega_o L_s} - \frac{v_p}{\omega_o L_s} - \frac{v_{cs}}{\omega_o L_s} \quad (2.35)$$

$$\frac{dv_p}{d(\omega_o t)} = \frac{i_s}{\omega_o C_p} - \frac{i_{lp}}{\omega_o C_p} - \frac{i_p}{\omega_o C_p} \quad (2.36)$$

$$\frac{dv_{cs}}{d(\omega_o t)} = \frac{i_s}{\omega_o C_s} \quad (2.37)$$

$$\frac{di_{lp}}{d(\omega_o t)} = \frac{v_p}{\omega_o L_p} \quad (2.38)$$

$$\frac{di_p}{d(\omega_0 t)} = \frac{v_p}{\omega_0 L_t} \quad (2.39)$$

Mode 3 is between  $\phi + \mu$  and  $\frac{\pi+\xi}{2}$  and the differential equations for this mode are obtained as

$$\frac{di_s}{d(\omega_0 t)} = \frac{V_i}{\omega_0 L_s} - \frac{v_p}{\omega_0 L_s} - \frac{v_{cs}}{\omega_0 L_s} \quad (2.40)$$

$$\frac{dv_p}{d(\omega_0 t)} = \frac{i_s}{\omega_0 C_p} - \frac{i_{ip}}{\omega_0 C_p} - \frac{I_{op}}{\omega_0 C_p} \quad (2.41)$$

$$\frac{dv_{cs}}{d(\omega_0 t)} = \frac{i_s}{\omega_0 C_s} \quad (2.42)$$

$$\frac{di_{ip}}{d(\omega_0 t)} = \frac{v_p}{\omega_0 L_p} \quad (2.43)$$

$$\frac{di_p}{d(\omega_0 t)} = 0 \quad (2.44)$$

Mode 4 lies between  $\frac{\pi+\xi}{2}$  and  $\pi + \phi$  and the differential equations for this mode are obtained as

$$\frac{di_s}{d(\omega_0 t)} = -\frac{v_p}{\omega_0 L_s} - \frac{v_{cs}}{\omega_0 L_s} \quad (2.45)$$

$$\frac{dv_p}{d(\omega_0 t)} = \frac{i_s}{\omega_0 C_p} - \frac{i_{ip}}{\omega_0 C_p} - \frac{I_{op}}{\omega_0 C_p} \quad (2.46)$$

$$\frac{dv_{cs}}{d(\omega_0 t)} = \frac{i_s}{\omega_0 C_s} \quad (2.47)$$

$$\frac{di_{ip}}{d(\omega_0 t)} = \frac{v_p}{\omega_0 L_p} \quad (2.48)$$

$$\frac{di_p}{d(\omega_0 t)} = 0 \quad (2.49)$$

These four sets of equations when solved, provide the first half cycle of the circuit waveforms. The second half can be similarly solved by just changing the sign of  $V_i$  and  $I_{sp}$  in the above sets of equations. The initial value of the state variables is set to zero and the four sets of equations are solved sequentially. The instantaneous values of the state variables at the end of one mode of operation are substituted as the initial values for the next set of equations. This is done for the four modes and then repeated for the next half cycle with the sign change.

### 2.5.2 Simulation results

In this section, simulation results are presented for two values of  $K_p$ , i.e.  $K_p = 2$  and  $K_p \approx 1$ . Figure 2.36 shows the first few cycles of operation for a capacitive parallel branch (i.e.,  $K_p = 2$ ). The series branch of the resonant circuit is kept tuned to the switching frequency of the converter. The figure shows the waveforms for all the state variables. It can be seen that the voltage across the series capacitor,  $v_{cs}$  rises to 3 p.u. during the second cycle of operation. Also the current through the parallel inductor goes to 2 p.u. during the same cycle. Although these values settle to less than 1.5 p.u. in the steady state, the transient values need to be considered in the selection of component ratings. Figures 2.37 and 2.38 show the waveforms after ten and twenty cycles of operation, respectively. Steady state is reached after approximately 20 cycles of operations.

Figures 2.39 to 2.41 show the transient waveforms for a nearly tuned parallel branch (i.e.,  $K_p \approx 1$ ). The waveforms in these figures are quite similar to the waveforms in Figs. 2.36 to 2.38. However, the steady state is reached after approximately thirty cycles. All these figures show that the circuit operates quite stably during the transient period. The circuit does not exhibit any drastic behaviour during the tran-

sient period, and the circuit variables settle down to the steady state values predicted by the frequency-domain analysis.

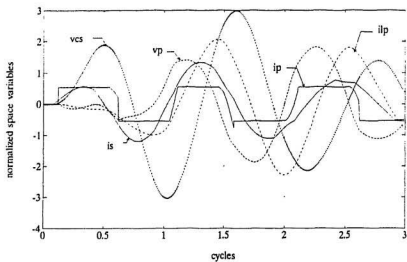


Figure 2.36: Transient waveforms for first few cycles of operation with  $K_p = 2$

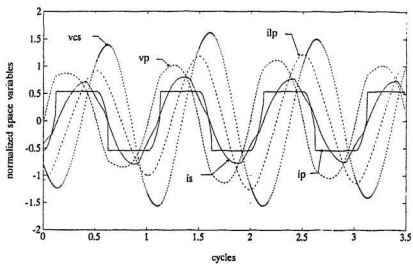


Figure 2.37: Transient waveforms after ten cycles of operation with  $K_p = 2$

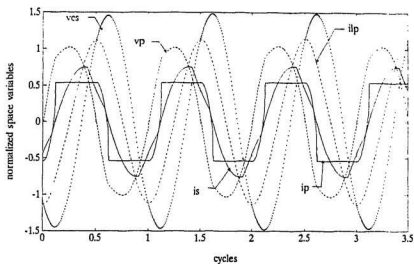


Figure 2.38: Transient waveforms after twenty cycles of operation with  $K_p = 2$

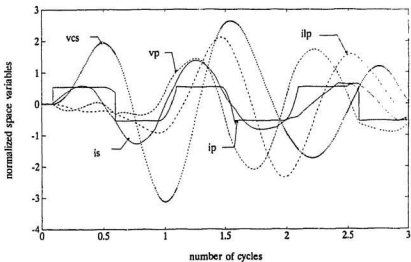


Figure 2.39: Transient waveforms for first few cycles of operation with  $K_p \approx 1$

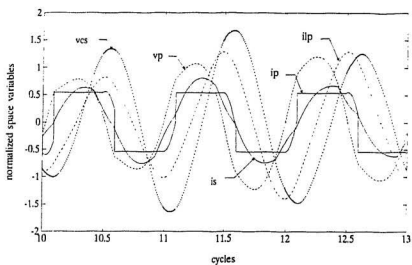


Figure 2.40: Transient waveforms after ten cycles of operation with  $K_p \approx 1$

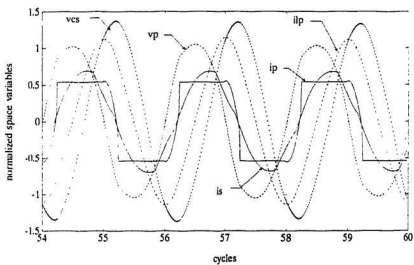


Figure 2.41: Transient waveforms at the end of thirty cycles of operation with  $K_p \approx 1$

## Chapter 3

# Series-Parallel Resonant Converter with Tertiary Winding Resonance

In this chapter, the model described in Chapter 2 is modified to study the series-parallel resonant converter with the parallel resonant circuit on a third winding of the high frequency transformer. Frequency-domain modeling and analysis are used to obtain generalized equations and performance curves for the steady-state operation and design of the converter.

### 3.1 Circuit description

Figure 3.1 shows the basic series-parallel resonant converter with a three winding transformer. The only difference between this circuit and the one discussed in the previous chapter is that the parallel resonant components  $L_p$  and  $C_p$  are placed on a tertiary winding of the high frequency transformer. The high-frequency transformer provides isolation as well as voltage transformation to get the required output voltage. The arrangement provides greater flexibility in the choice of the parallel capacitor,  $C_p$ . By reducing the current carrying capacity of the parallel inductor,  $L_p$ , its size can

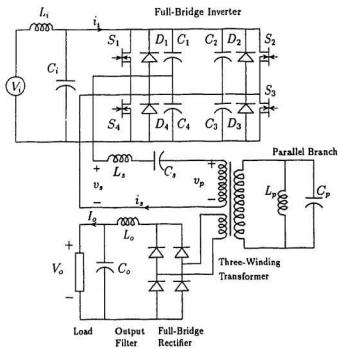


Figure 3.1: Circuit diagram of the dc/dc resonant converter

also be reduced significantly. Another advantage of using a three-winding transformer is that the leakage inductance of the transformer gets divided into three parts: the primary leakage is compensated for by the series inductor; the leakage of the tertiary winding comes in series with the parallel components when referred to the primary, and it does not contribute to the drop in output voltage; the secondary leakage at the input of the full-bridge rectifier causes the commutation overlap. Due to the lower leakage inductance of the three winding transformer, this converter is more suitable for high frequency operation.

### 3.2 Frequency-domain model

Figure 3.2 shows the  $n$ th harmonic equivalent circuit of the converter. The input voltage,  $v_{2n}$ , to the resonant circuit is the  $n$ th harmonic component of the PWM voltage,  $v_s$ . The output of the converter is modelled as a current source,  $i_p$ , which is assumed to be trapezoidal due to the presence of the leakage reactance,  $X_l$ , of the secondary winding.  $i_{pn}$  is the  $n$ th harmonic component of  $i_p$ . When referred to the primary, the leakage reactance of the tertiary winding,  $X_t$ , appears in series with the parallel resonant circuit parameters  $X_{lp}$  and  $X_{cp}$ , and therefore does not contribute to the voltage drop at the output. The leakage inductance of the primary winding is included in the series inductor,  $L_s$ .

$X_t'$ ,  $X_{cp}'$  and  $X_{lp}'$  are the reactances on the tertiary side and  $X_l'$  is the leakage reactance on the secondary side.

### 3.3 Steady-state analysis of the converter

In this section, the steady-state analysis of the converter, using the frequency-domain model, developed in Fig. 3.2, is presented. Generalized equations are developed, and

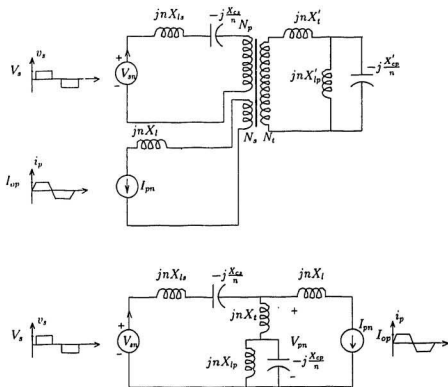


Figure 3.2:  $n$ th harmonic equivalent circuit of the converter

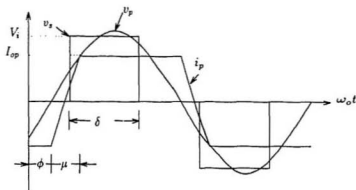


Figure 3.3: Generalized waveforms of the dc/dc resonant converter

a procedure for obtaining the steady-state performance of the converter is described. The simplifying assumptions outlined in Section 2.3.1 apply to this analysis.

### 3.3.1 Frequency-domain analysis

Figure 3.3 shows the generalized steady-state waveforms of the input voltage,  $v_s$ , output voltage,  $v_p$ , and the output current,  $i_p$ . These waveforms remain the same for both the primary and secondary side resonant circuits. This is because the leakage reactance of the tertiary winding,  $X_t$ , is very small and therefore does not affect the performance of the converter significantly. The angle,  $\phi$ , is the phase difference between the fundamental component of the PWM voltage,  $v_s$ , and the transformer primary voltage,  $v_p$ . Angle,  $\delta$ , is the pulse width of  $v_s$ , and  $\mu$ , is the commutation angle.

The normalized equations for the  $n$ th harmonic component of  $v_s$ ,  $v_p$ ,  $i_s$  and  $i_p$  are the same as in the preceding chapter and are reproduced here for convenience.

$$v_{snN} = \frac{4}{n\pi} \sin\left(\frac{n\pi}{2}\right) \sin\left(\frac{n\delta}{2}\right) \sin(n\omega_o t) \quad (3.1)$$

$$i_{pnN} = \frac{8I_{opN}}{\pi\mu n^2} \sin\left(\frac{n\mu}{2}\right) \sin\left[n\left(\omega_o t - \phi - \frac{\mu}{2}\right)\right] \quad (3.2)$$

$$i_{snN} = \frac{4}{n\pi Z_{in}} \sin\left(\frac{n\pi}{2}\right) \cos(n\omega_o t) + \dots \\ + \frac{8I_{opN}}{\pi\mu n^2} \sin\left(\frac{n\mu}{2}\right) \sin\left[n\left(\omega_o t - \phi - \frac{\mu}{2}\right)\right] \frac{Z_{pnN}}{Z_{inN}} \quad (3.3)$$

$$v_{pnN} = \frac{4Z_{pnN}}{n\pi Z_{inN}} \sin\left(\frac{n\pi}{2}\right) \sin\left(\frac{n\delta}{2}\right) \sin(n\omega_o t) + \dots \\ + \frac{8I_{opN}}{\pi\mu n^2} \sin\left(\frac{n\mu}{2}\right) \cos\left[n\left(\omega_o t - \phi - \frac{\mu}{2}\right)\right] \frac{Z_{pnN}Z_{snN}}{Z_{inN}} \quad (3.4)$$

where

$$Z_{sn} = j\left(nX_{ls} - \frac{X_{cs}}{n}\right) \quad (3.5)$$

$$Z_{pn} = jnX_{lp} - j\frac{X_{lp}X_{cp}}{nX_{lp} - \frac{X_{cp}}{n}} \quad (3.6)$$

$$Z_{in} = Z_{sn} + Z_{pn} \quad (3.7)$$

Although Equations 3.1 to 3.4 contain the same unknown parameters,  $\phi$ ,  $\mu$ , and  $I_{opN}$ , as in the corresponding equations in chapter 2, a slightly modified procedure is adopted to determine these parameters.

### 3.3.2 Solution of equations

Three equations are required to obtain a unique solution for  $\phi$ ,  $\mu$  and  $I_{opN}$ . The first equation is obtained from the condition that  $v_p = 0$  at  $\omega_o t = \phi$ . From equation 3.4 the following equation is obtained.

$$\begin{aligned} & \sum_{n=1,3,\dots}^{\infty} \frac{4}{n\pi} \sin\left(\frac{n\pi}{2}\right) \sin\left(\frac{n\delta}{2}\right) \sin(n\phi) \frac{Z_{pn}}{Z_{in}} + \dots \\ & + \sum_{n=1,3,\dots}^{\infty} \frac{8I_{opN}}{\pi\mu n^2} \sin\left(\frac{n\mu}{2}\right) \cos\left(\frac{n\mu}{2}\right) \frac{Z_{pn}Z_{sn}}{Z_{in}} = 0 \end{aligned} \quad (3.8)$$

The second equation is obtained from the condition that the normalized output voltage  $V_{opN}$  referred to the primary is equal to the normalized primary current  $I_{opN}$  and can be written as the average of  $v_p$  over the interval  $\phi + \mu$  to  $\phi + \pi$ .

$$\begin{aligned} V_{opN} &= \frac{1}{\pi} \int_{\phi+\mu}^{\phi+\pi} v_p d\omega_o t \\ &= \sum_{n=1,3,\dots}^{\infty} \frac{4}{\pi^2 n^2} \sin\left(\frac{n\pi}{2}\right) \sin\left(\frac{n\delta}{2}\right) \frac{Z_{pn}}{Z_{in}} \dots \\ & \quad \cdot [\cos(n(\phi + \mu)) + \cos(n\phi)] \end{aligned} \quad (3.9)$$

In Chapter 2,  $v_p$ , the voltage at the primary of the transformer was assumed to be sinusoidal. For the present circuit,  $v_p$  can no longer be assumed sinusoidal due to the presence of the leakage reactance of the tertiary winding,  $X_t$ . The complete general expression for  $v_p$  is therefore used to derive the expression for the commutation

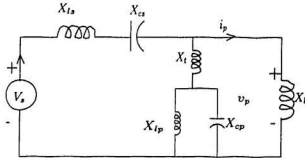


Figure 3.4: Equivalent circuit during the commutation period  $\mu$

angle,  $\mu$  as follows. During the commutation interval,  $\mu$ , the equivalent circuit of the converter is as shown in Fig. 3.4. The following equation is obtained.

$$\frac{di_p}{d(\omega_o t)} = \frac{v_p}{X_{L1}}, \quad \text{for } \phi \leq \omega_o t \leq \phi + \mu \quad (3.10)$$

Taking the integral of Equation 3.10 gives

$$\begin{aligned} i_p &= \frac{1}{X_{L1}} \int v_p d(\omega_o t) \\ &= \frac{1}{X_{L1}} \sum_{n=1,3,\dots}^{\infty} \frac{4}{\pi^2 n^3} \sin\left(\frac{n\pi}{2}\right) \sin\left(\frac{n\delta}{2}\right) [-\cos(n\omega_o t)] \frac{Z_{pn}}{Z_{in}} \dots \\ &\quad + \frac{1}{X_{L1}} \sum_{n=1,3,\dots}^{\infty} \frac{8}{\pi \mu n^4} I_{opN} \frac{Z_{sn} Z_{pn}}{Z_{in}} \sin\left(\frac{n\mu}{2}\right) \sin\left[n\left(\omega_o t - \phi - \frac{\mu}{2}\right)\right] + K \end{aligned} \quad (3.11)$$

where  $K$  is a constant of integration. Now using the conditions that,  $i_p = -I_{opN}$  at  $\omega_o t = \phi$  and  $i_p = I_{opN}$  at  $\omega_o t = \phi + \mu$  the following equations are obtained.

$$\begin{aligned}
 -I_{opN} &= \frac{1}{X_I} \sum_{n=1,3,\dots}^{\infty} \frac{4}{\pi^2 n^3} \sin\left(\frac{n\pi}{2}\right) \sin\left(\frac{n\delta}{2}\right) [-\cos(n\phi)] \frac{Z_{pn}}{Z_{in}} \dots \\
 &\quad - \frac{1}{X_I} \sum_{n=1,3,\dots}^{\infty} \frac{8}{\pi \mu n^4} I_{opN} \frac{Z_{sn} Z_{pn}}{Z_{in}} \sin^2\left(\frac{n\mu}{2}\right) + K \quad (3.12)
 \end{aligned}$$

$$\begin{aligned}
 I_{opN} &= \frac{1}{X_I} \sum_{n=1,3,\dots}^{\infty} \frac{4}{\pi^2 n^3} \sin\left(\frac{n\pi}{2}\right) \sin\left(\frac{n\delta}{2}\right) [-\cos((n\phi + \mu))] \frac{Z_{pn}}{Z_{in}} \dots \\
 &\quad + \frac{1}{X_I} \sum_{n=1,3,\dots}^{\infty} \frac{8}{\pi \mu n^4} I_{opN} \frac{Z_{sn} Z_{pn}}{Z_{in}} \sin^2\left(\frac{n\mu}{2}\right) + K \quad (3.13)
 \end{aligned}$$

Subtracting equation 3.12 from equation 3.13 gives,

$$\begin{aligned}
 2I_{opN} &= \frac{1}{X_I} \sum_{n=1,3,\dots}^{\infty} \frac{4}{\pi^2 n^3} \sin\left(\frac{n\pi}{2}\right) \sin\left(\frac{n\delta}{2}\right) [\cos(n\phi) - \cos((n\phi + \mu))] \frac{Z_{pn}}{Z_{in}} \dots \\
 &\quad + \frac{1}{X_I} \sum_{n=1,3,\dots}^{\infty} \frac{16}{\pi \mu n^4} I_{opN} \frac{Z_{sn} Z_{pn}}{Z_{in}} \sin^2\left(\frac{n\mu}{2}\right) \quad (3.14)
 \end{aligned}$$

For given circuit parameters and pulse width,  $\delta$ , Equations 3.8, 3.9 and 3.14 are solved for  $\phi$ ,  $\mu$  and  $I_{opN}$ . After finding the values of  $\phi$ ,  $\mu$  and  $I_{opN}$ , the generalized equations of the converter (Equations 3.1 to 3.4) are employed to obtain various circuit variables and to investigate the effect of circuit parameters on the performance of the converter.

### 3.4 Steady-state performance

The simulated waveforms for  $v_s$ ,  $v_p$ ,  $i_s$  and  $i_p$  are shown in Fig. 3.5 to 3.10 for variations in  $K_p$  and  $K_s$ . Figures 3.5 and 3.6 show the waveforms for tuned series and parallel resonant branches. Figure 3.5 ( $\delta = 114^\circ$ ) shows that the voltage across the tertiary winding referred to the primary,  $v_p$ , is at zero phase and its peak value is about 1.15 p.u. The resonant current,  $i_s$ , is quite small and the converter is expected to have low losses.

Figure 3.6 shows the operation for  $\delta = 65^\circ$ . This value is chosen to compare the simulation result with the experimental result when the converter is operated at a higher dc input voltage,  $V_i$ . As shown, the series resonant current,  $i_s$ , is more distorted. The efficiency when operating at a higher input voltage is expected to be lower.

Figure 3.7 shows the waveforms for an inductive parallel branch (i.e.,  $K_p = 0.5$ ) and tuned series branch (i.e.,  $K_s = 1$ ). In this case, the waveform for  $v_p$  remains almost the same but the resonant current,  $i_s$ , has increased significantly. Also the resonant current leads the input voltage,  $v_s$ , resulting in high switching losses.

Figure 3.8 shows the waveforms for a capacitive parallel branch (i.e.,  $K_p = 2$ ). The resonant current,  $i_s$ , is very high but lags the input voltage. Also the voltage waveform is very much distorted.

Figure 3.9 shows the circuit waveforms for an inductive series branch (i.e.,  $K_s = 0.6$ ). In this mode of operation,  $v_p$  and  $i_s$  lead the input voltage,  $v_s$ . Figure 3.10 shows the waveforms for a capacitive series branch (i.e.,  $K_s = 1.4$ ). In this case, both  $v_p$  and  $i_s$ , lag behind the input voltage,  $v_s$ . Also the voltage,  $v_p$ , is smaller; its peak is approximately 0.9 p.u.

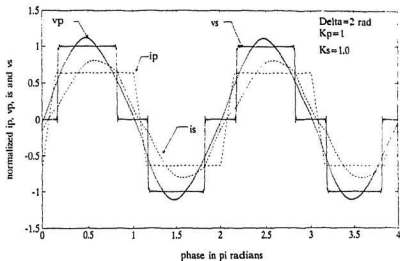


Figure 3.5: Simulated waveforms of the converter for tuned series and parallel branch,  $\delta = 114^\circ$

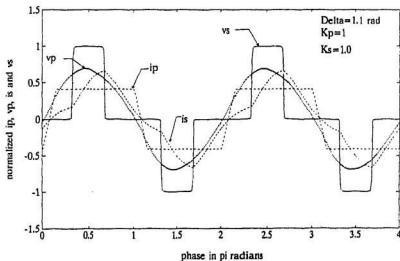


Figure 3.6: Simulated waveforms of the converter for tuned series and parallel branches,  $\delta = 65^\circ$

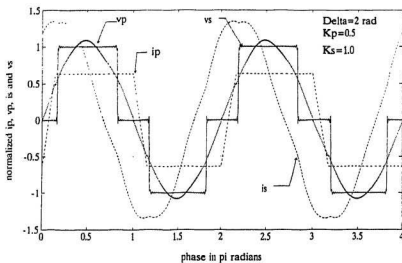


Figure 3.7: Simulated waveforms of the converter for inductive parallel branch

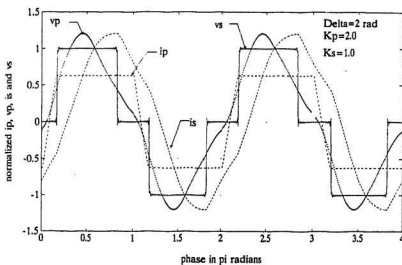


Figure 3.8: Simulated waveforms of the converter for capacitive parallel branch

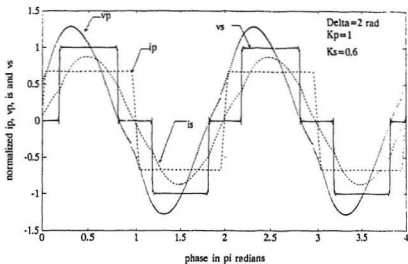


Figure 3.9: Simulated waveforms of the converter for inductive series branch

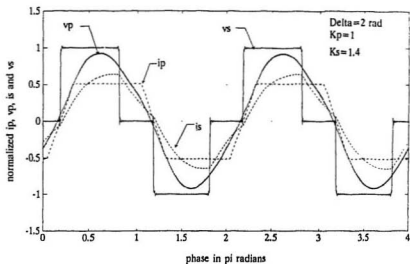


Figure 3.10: Simulated waveforms of the converter for capacitive series branch

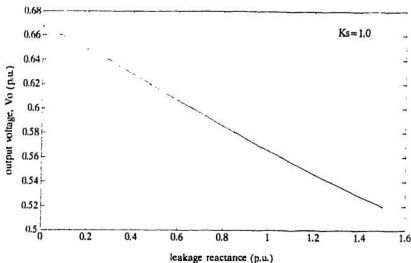


Figure 3.11: Output voltage  $V_o$  vs. leakage reactance for tuned series branch

Figure 3.11 shows the effect of the leakage reactance,  $X_l$ , on the output voltage,  $V_o$ . The figure shows that the output voltage decreases as the leakage reactance increases. This drop is not as significant in the three winding transformer as it is in the two winding transformer discussed in Chapter 2, because the leakage reactance in this transformer is about one-third. Therefore, this converter is expected to show better performance.

Figure 3.12 shows the variation in output voltage with switching frequency. The output voltage,  $V_o$ , decreases steadily as the switching frequency is increased. It should be noted that the variation in  $V_o$  when  $f_s$  is varied from 1 p.u. to 10 p.u. is approximately 1 p.u., which is much less than the variation in  $V_o$ , in the converter with primary resonance. Therefore, this converter is more suitable for operation at higher frequency.

Figure 3.13 shows the variation of  $V_o$  with the load,  $R_l$ , for different values of  $K_s$  and a tuned parallel branch ( $K_p \approx 1$ ). The figure shows that as the series branch

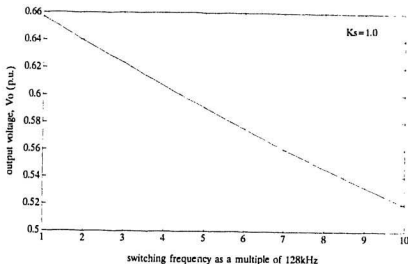


Figure 3.12:  $V_o$  vs. switching frequency,  $f_s$

becomes more capacitive (i.e.,  $K_s > 1$ ) the variation in output voltage increases with load. There is negligible variation in the output voltage with load when the series branch is tuned. Therefore, to maintain constant output voltage with varying load, it is desirable to keep the series circuit tuned.

Figure 3.14 shows a similar plot for a capacitive parallel branch (i.e.,  $K_p = 2$ ). It can be seen that there is large variation in  $V_o$  for  $K_s > 1$ , whereas it is constant for  $K_s = 1$ . The output voltage for  $K_s > 1$  is higher than that at  $K_s = 1$  when the parallel branch is capacitive.

Figure 3.15 shows the variation of resonant current,  $i_s$ , with  $K_p$  for different values of  $X_{cp}$ . The figure shows that the resonant current increases as  $K_p$  increases. This increase is very small for higher values of  $X_{cp}$ . Higher resonant current means higher losses. Therefore, if the converter has to be operated at higher values of  $K_p$ ,  $X_{cp}$  should be kept high.

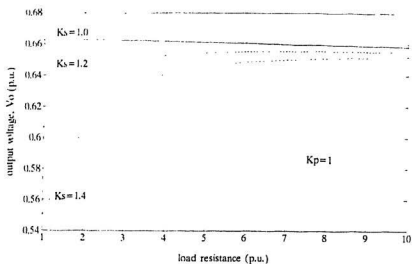


Figure 3.13:  $V_o$  vs. load resistance  $R_l$  with tuned parallel branch

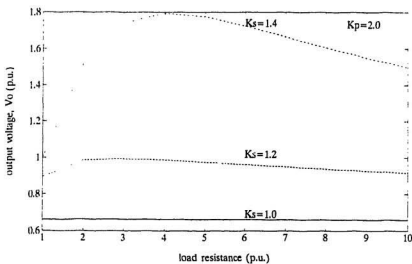


Figure 3.14:  $V_o$  vs. load resistance  $R_l$  with capacitive parallel branch

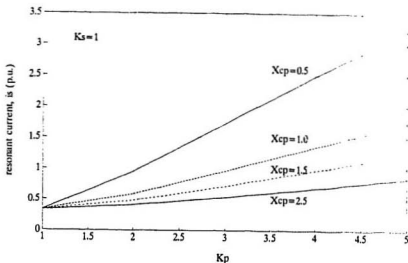


Figure 3.15: Resonant current,  $i_s$  vs.  $K_p$  for different values of  $X_{cp}$ .

Figure 3.16 shows the variation of the minimum value of  $\delta$  with  $K_p$  for different values of parallel capacitive reactance,  $X_{cp}$ . It can be seen from the figure that as  $K_p$  increases, the value of  $\delta_{\min}$  decreases, resulting in wider range of variation of  $\delta$ . The effect of increasing  $X_{cp}$  is to increase the value of  $\delta_{\min}$ . Therefore if a variation in the output voltage is desired, a lower value of  $X_{cp}$  should be chosen.

Figure 3.17 shows the total harmonic distortion of  $v_p$  for variation in the series reactance,  $X_{Ls}$ . The curve is drawn for variation in parallel reactance,  $X_{Lp}$ . The % THD decreases slightly with increasing  $X_{Ls}$  but increases with  $X_{Lp}$ . When compared with Fig. 2.31 for primary side resonant converter, it can be seen that for similar values of series and parallel reactance the variation in % THD with series reactance is much more in Fig. 3.17. Also the % THD is higher in this case. The increase in %THD is due to the presence of the leakage reactance,  $X_l$ .

Figures 3.18 shows that the total harmonic distortion is very high for small values of  $K_l$ , where  $K_l$  is the ratio of series reactance,  $X_{Ls}$  to parallel reactance,  $X_{Lp}$ , i.e.,

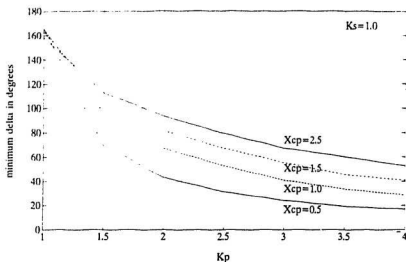


Figure 3.16: Variation of  $\delta_{min}$  with  $K_p$  for different values of  $X_{cp}$ .

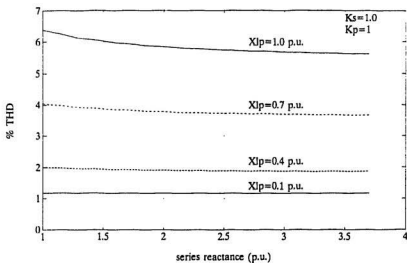


Figure 3.17: Total harmonic distortion with  $X_{lp}$ , with tuned series and parallel branch

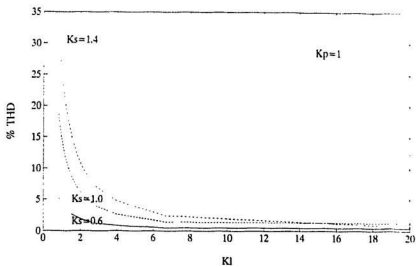


Figure 3.18: Total harmonic distortion with  $K_I$  for  $K_s=0.6, 1.0$  and  $1.4$  for tuned parallel branch

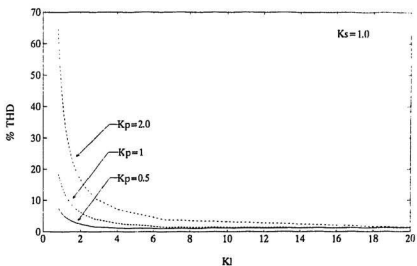


Figure 3.19: Total harmonic distortion with  $K_I$  for  $K_p=0.5, 1$  and  $2.0$

$K_I = X_{Ls}/X_{Lp}$ . The % THD decreases rapidly as  $K_I$  increases.

### 3.5 Series-parallel resonant converter with integrated magnetics

The requirement for reduced size is an important consideration in converter design. In the series-parallel converter, the inductors  $L_s$  and  $L_p$  take up a lot of space on the converter. In order to reduce the size of the converter further, the magnetics of the converter with the three winding transformer may be integrated. In this arrangement, the series branch inductance  $L_s$  and the parallel branch inductance  $L_p$  are integrated into the three winding transformer. In this section, a model is developed for the converter with integrated magnetics. Again the modeling is done in the frequency domain using the same approach as the one already presented in this chapter. Figure 3.20 shows the equivalent circuit of the three winding transformer with integrated magnetics. The leakage inductance of the tertiary winding comes in series with the capacitor,  $C_p$ , when referred to the primary of the transformer. The leakage inductance of the secondary winding,  $L_l$ , remains the same. The primary side leakage inductance is compensated by the series inductor,  $L_s$ , which is now a composite part of the transformer. The magnetizing inductances of the converter are assumed to be negligible.

The analysis procedure for the integrated magnetics converter is the same as the analysis presented in Section 3.3. The generalized equations (Equations 3.1 to 3.4) apply to the equivalent circuit of Fig. 3.20. The resonant circuit impedances for this circuit are given by

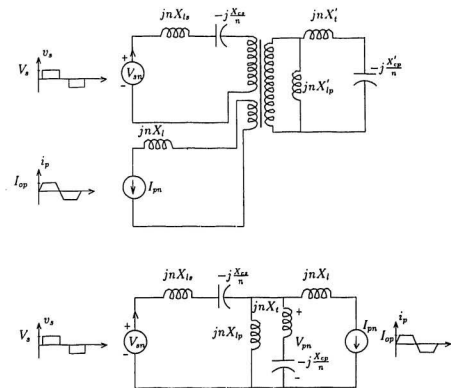


Figure 3.20:  $n$ th harmonic equivalent circuit for an integrated series-parallel resonant converter

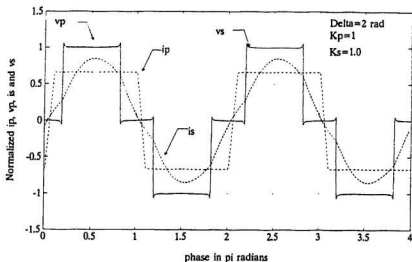


Figure 3.21: Simulated waveforms for a converter with integrated magnetics,  $\delta = 114^\circ$

$$Z_{sn} = j \left( nX_{ls} - \frac{X_{Cs}}{n} \right) \quad (3.15)$$

$$Z_{pn} = j \frac{nX_{lp} (nX_{ls} - \frac{X_{Cs}}{n})}{nX_{ls} + nX_{lp} - \frac{X_{Cs}}{n}} \quad (3.16)$$

$$Z_{in} = Z_{sn} + Z_{pn} \quad (3.17)$$

Figure 3.21 and 3.22 show the simulated waveforms for this converter. It can be seen that the waveforms are quite similar to those in Fig. 3.5 and 3.6. The performance of the converter with integrated magnetics is the same as the converter described in Section 3.4. However because of integration there are no external physical resonant inductors, with the associated requirement for space. Consequently the size of the converter is reduced.

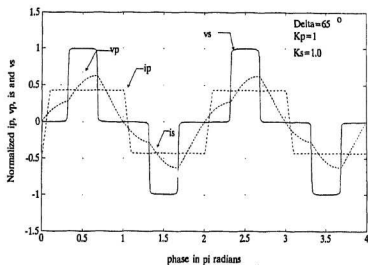


Figure 3.22: Simulated waveforms for a converter with integrated magnetics,  $\delta = 65^\circ$

## Chapter 4

# Design Example and Experimental Results

In this chapter, a design example is presented for a series-parallel resonant converter with the parallel branch on the third winding of the transformer. The example is developed using the performance curves presented in the previous chapter. Experimental results for the two types of resonant converters discussed in Chapters 2 and 3 are presented and comparison is made between the simulation and the experimental results.

### 4.1 Design example

A design example is presented to illustrate the use of performance curves to design the resonant converter. Using the converter described in Chapter 3, a procedure for determining the resonant converter parameters and the tradeoffs required are outlined. The example chosen represents the power supply for a telecommunications equipment. The following are the specifications for the converter.

Input voltage, $V_i$	=	48V
Operating frequency, $f_o$	=	128kHz
Output voltage, $V_o$	=	5V
Output Current, $I_o$	=	100 Amps

The following base quantities are chosen

Base voltage, $V_{base}$	=	$V_i$	=	48V
Base impedance, $Z_{base}$	=	$R_l$	=	0.05 $\Omega$
Base frequency, $f_{base}$	=	$f_s$	=	128kHz

To obtain the specified output voltage the primary to secondary turns ratio ( $N_p : N_s$ ) of the transformer is taken to be 6:1. The primary to tertiary turns ratio ( $N_p : N_t$ ) is chosen to be 1:2. For the above specifications the load resistance is 0.05  $\Omega$ , which corresponds to 1.8  $\Omega$  when referred to the primary. The expected output voltage referred to the primary,  $V_{op}$  is obtained as

$$V_{op} = \frac{5 \times 6}{48} = 0.625 \text{ p.u.}$$

The first step in the design is to select suitable values for  $K_s$  and  $K_p$ . Figures 3.13 and 3.14 show that there is no voltage regulation if the series resonant circuit is tuned (i.e.,  $K_s = 1$ ). Thus to keep the output voltage constant for varying load,  $K_s$  is chosen to be 1, i.e. the series resonant circuit is tuned to the operating frequency. Figure 3.15 shows the variation of the resonant current,  $i_s$  with  $K_p$ , for different values of  $X_{cp}$ .

From this plot, it can be seen that as  $K_p$  increases the resonant current increases and the losses in the converter increase. Therefore,  $K_p$  has to be kept low. However, fig. 3.16 shows that lower values of  $K_p$  result in smaller range of variation in  $\delta$ . In order to allow for a wider range of variation in  $\delta$  and hence a wider variation in output voltage, and yet keep the resonant current low,  $K_p$  is chosen to be 1.5 and  $X_{cp}$  is chosen to be 1 p.u.

For these values of  $K_p$  and  $X_{cp}$  the parallel inductance,  $L_p$ , is calculated from,

$$\begin{aligned} X_{lp} &= \frac{X_{cp}}{K_p} \\ &= \frac{1 \times 1.8}{1.5} \\ &= 1.2\Omega \end{aligned} \quad (4.1)$$

The parallel inductive reactance referred to the tertiary side is given by

$$\begin{aligned} X'_{lp} &= \left( \frac{N_t}{N_p} \right)^2 \times X_{lp} \\ &= 4 \times 1.2 \\ &= 4.8\Omega \end{aligned} \quad (4.2)$$

and

$$\begin{aligned} L_p &= \frac{X'_{lp}}{2\pi f} \\ &= \frac{4.8}{2\pi \times 128 \times 10^3} \\ &\approx 6\mu H \end{aligned} \quad (4.3)$$

Similarly, the parallel capacitance,  $C_p$ , is calculated as follows.

$$X'_{cp} = \frac{1}{2\pi f C_p} \quad (4.4)$$

or

$$\begin{aligned} C_p &= \frac{1}{2\pi f X'_{cp}} = \frac{1}{2\pi f \left(\frac{N_s}{N_p}\right)^2 X_{cp}} \\ &= \frac{1}{2\pi \times 128 \times 10^3 \times 4 \times 1.8} \\ &= 0.17 \mu f \end{aligned} \quad (4.5)$$

The values of the series components are restricted by the size. Also, as discussed in the previous chapter, to obtain a sinusoidal voltage across the primary of the transformer the ratio,  $K_l$  must be at least 2. Therefore, in order to satisfy both conditions, the value of  $X_{ls}$  is chosen to be 2 p.u. The value of  $L_s$  is calculated as follows.

$$\begin{aligned} L_s &= \frac{X_{ls}}{2\pi f} \\ &= \frac{2 \times 1.8}{2\pi \cdot 128 \times 10^6} \\ &= 4.5 \mu H \end{aligned} \quad (4.6)$$

Similarly, for  $K_s = 1$ ,  $X_{cs} = 2$  p.u. and  $C_s$  is calculated as follows.

$$\begin{aligned} C_s &= \frac{1}{2\pi f X_{cs}} \\ &= \frac{1}{2\pi \times 128 \times 10^3 \times 2 \times 1.8} \\ &= 0.35 \mu f \end{aligned} \quad (4.7)$$

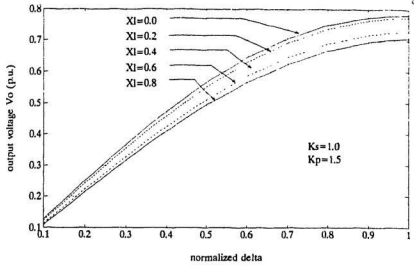


Figure 4.1: Output voltage,  $V_o$  vs.  $\delta$

Figure 4.1 shows the variation in output voltage,  $V_o$  with  $\delta$  for different values of transformer leakage reactance,  $X_l$ . Depending on the value of transformer leakage the value of the pulse width,  $\delta$ , which yields the required output, can be found. A practical value for the leakage reactance of a three winding transformer would be 0.45 p.u. For this value of leakage reactance, the value of  $\delta$  to obtain  $V_o = 0.625$  p.u. is found from Fig. 4.1 to be 0.62 p.u. or  $112^\circ$ . The leakage reactance of 0.45 p.u. results in

$$X_l = 0.45 \times 1.8 = 0.81 \Omega$$

and

$$\begin{aligned}
 L_l &= \frac{X_l}{2\pi f} & (4.8) \\
 &= \frac{0.81}{2\pi \times 128 \times 10^3} \\
 &\approx 1\mu H
 \end{aligned}$$

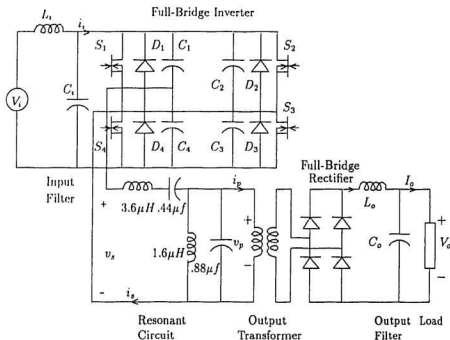


Figure 4.2: Experimental setup for the series-parallel resonant converter with primary resonance

## 4.2 Experimental results

In this section, experimental results for the two types of converters namely, primary resonant converter and the tertiary resonant converter are presented. It is shown that the models accurately describe the converters. The experiments were performed in the power lab of Bell-Northern Research, Ottawa. The two converters were designed and developed by the power group at BNR.

### 4.2.1 Primary resonant converter

The experimental setup for the series-parallel resonant converter with primary resonance is shown in fig. 4.2. The following are the circuit specifications,

Input Voltage, $V_i$	=	40V to 60V
Output Voltage, $V_o$	=	5V
Output Current, $I_o$	=	100A
Operating frequency, $f_s$	=	128kHz

The full-bridge inverter comprises of eight IRFP 150 MOSFETs. Each switch consists of two MOSFETs in parallel to reduce the internal resistance of the switch. The control method used is the phase shift modulation and a modified Micro Linear soft switching control chip, ML4818 is used for the purpose. Switches  $S_2$  and  $S_3$  are always turned-on at zero-voltage and turned-off at zero-current. Snubber capacitors are used to achieve turn-off under zero-voltage. Switches  $S_1$  and  $S_4$  are turned-off at full voltage. The diodes used in the full-bridge rectifier are high frequency low recovery time diodes.

The series and the parallel, branches of the resonant circuit are tuned to the switching frequency. The power transformer has a primary to secondary turns ratio of 5:1. The transformer uses a horizontal ferrite core. Ferrite core has the advantage of low core losses at high ac flux densities and high frequencies.

The values of circuit components are as follows:

Series Inductance, $L_s$	=	$3.6\mu H$
Series Capacitance, $C_s$	=	$0.44\mu f$
Parallel Inductance, $L_p$	=	$1.6\mu H$
Parallel Capacitance, $C_p$	=	$0.88\mu f$

First, the converter was operated under varying load conditions and input voltage,  $V_i = 40V$ . Table 4.2.1 shows the input and output current and voltage values for this experiment. The efficiency of the converter was calculated at each stage. This experiment was repeated for  $V_i = 60V$  and Table 4.2.1 shows the results. Figure 4.3 shows the variation in efficiency with load. The converter has an efficiency around 80% from 20% to full load, for operation at 40V and 60V. The efficiency is slightly lower for 60V. Peak efficiency is achieved at approximately half load.

Figures 4.4 to 4.19 show the comparison between the simulated and the experimental waveforms. The waveforms show close agreement in shape and magnitude thus confirming the model and analysis procedure.

Figures 4.20 to 4.25 show the experimental waveforms for drain to source voltage,  $v_{ds}$ , voltage across diode rectifier,  $v_{dr}$ , and current through the secondary transformer winding,  $i'_p$ .

S. No.	$V_i$ (volts)	$I_i$ (amps)	$V_o$ (volts)	$I_o$ (amps)	Efficiency %
1.	40	0.3	5.14	0	0
2.	40	1.7	5.13	9.93	74.91
3.	40	3.1	5.13	20.0	82.74
4.	40	4.6	5.13	30.0	83.64
5.	40	6.1	5.12	40.0	83.93
6.	40	7.6	5.12	50.0	84.21
7.	40	9.2	5.12	60.0	83.47
8.	40	10.7	5.11	70.0	83.57
9.	40	12.3	5.11	80.0	83.09
10.	40	14.0	5.11	90.0	82.13
11.	40	15.7	5.10	100.0	81.21
12.	40	17.5	5.09	110.0	79.99

Table 4.1: Experimental results showing efficiency with variation in load for  $V_i = 40V$ 

S. No.	$V_i$ (volts)	$I_i$ (amps)	$V_o$ (volts)	$I_o$ (amps)	Efficiency %
1.	60	0.3	5.14	0	0
2.	60	1.2	5.14	10	71.39
3.	60	2.1	5.13	20	81.43
4.	60	3.1	5.13	30	82.74
5.	60	4.2	5.13	40	81.43
6.	60	5.3	5.12	50	80.50
7.	60	6.4	5.12	60	80.00
8.	60	7.5	5.12	70	79.64
9.	60	8.6	5.12	80	79.38
10.	60	9.8	5.11	90	78.21
11.	60	11.0	5.11	100	77.42
12.	60	12.2	5.10	110	76.64

Table 4.2: Experimental results showing efficiency with variation in load for  $V_i = 60V$

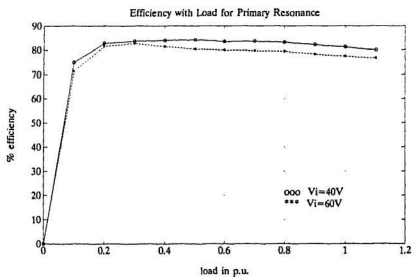


Figure 4.3: Efficiency with load for  $V_i = 40V$  and  $60V$

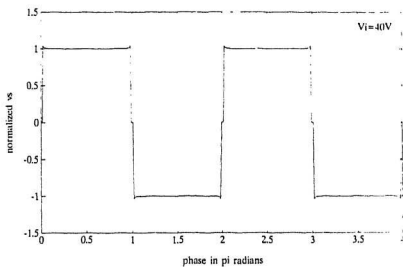


Figure 4.4: Simulated phase-shift modulated input voltage,  $v_s$ , for  $V_i = 40V$  and  $\delta = 175^\circ$

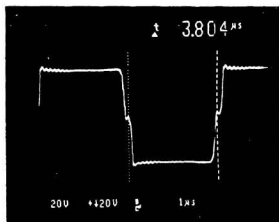


Figure 4.5: Experimental PSM input voltage,  $v_s$ , for  $V_i = 40V$

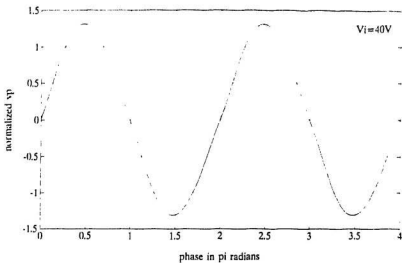


Figure 4.6: Simulated primary voltage,  $v_p$ , for  $V_i = 40V$

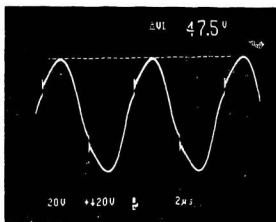


Figure 4.7: Experimental primary voltage,  $v_p$ , for  $V_i = 40V$

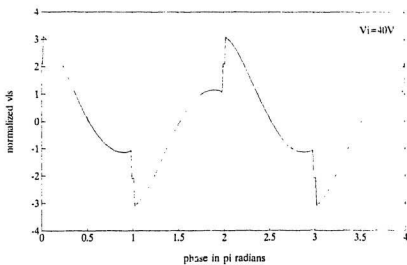


Figure 4.8: Simulated  $v_{I_s}$  for  $V_i = 40V$

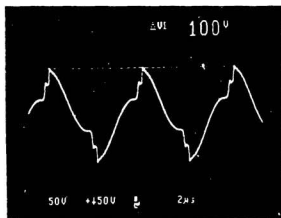


Figure 4.9: Experimental  $v_{I_s}$  for  $V_i = 40V$

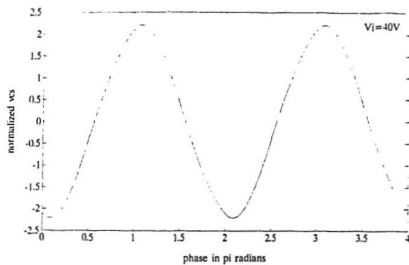


Figure 4.10: Simulated  $v_{cs}$  for  $V_i = 40V$

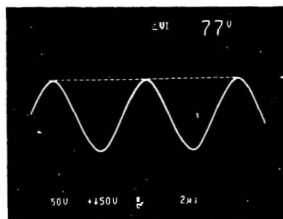


Figure 4.11: Experimental  $v_{cs}$  for  $V_i = 40V$

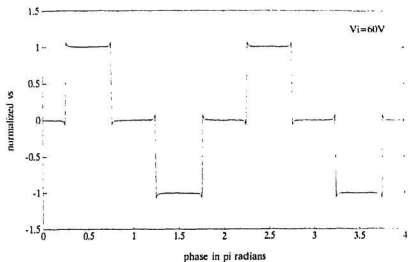


Figure 4.12: Simulated phase shift modulated input voltage,  $v$ , for  $V_i = 60V$ ,  $\delta = 114^\circ$

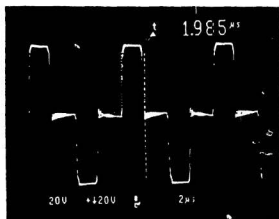


Figure 4.13: Experimental PSM input voltage,  $v$ , for  $V_i = 60V$

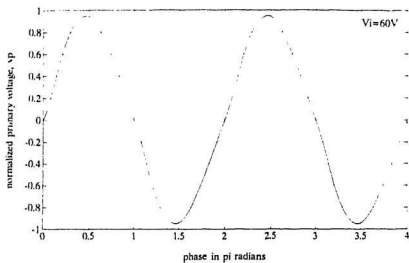


Figure 4.14: Simulated primary voltage,  $v_p$  for  $V_i = 60V$

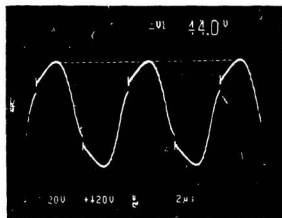


Figure 4.15: Experimental primary voltage,  $v_p$  for  $V_i = 60V$

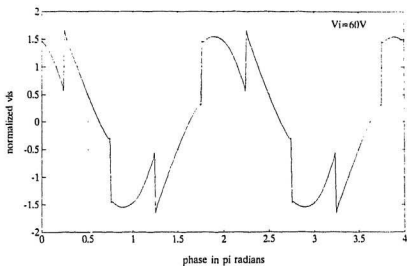


Figure 4.16: Simulated  $v_{i_s}$  for  $V_i = 60V$

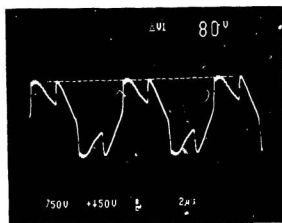


Figure 4.17: Experimental  $v_{i_s}$  for  $V_i = 60V$

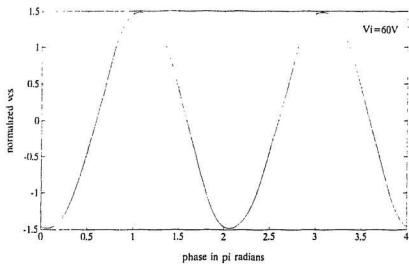


Figure 4.18: Simulated  $v_{cs}$  for  $V_i = 60V$

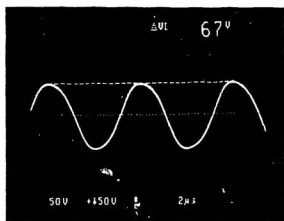


Figure 4.19: Experimental  $v_{cs}$  for  $V_i = 60V$

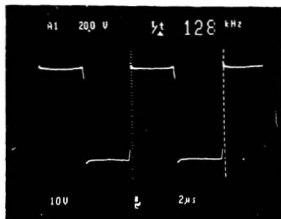


Figure 4.20: Experimental drain to source voltage  $v_d$ , for  $V_i = 40V$

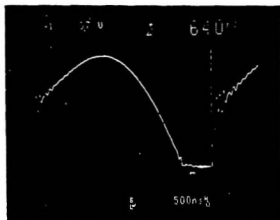


Figure 4.21: Experimental voltage across the diode rectifier,  $v_d$ , for  $V_i = 40V$

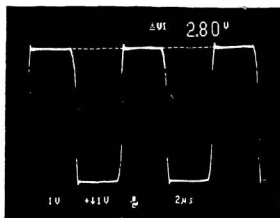


Figure 4.22: Experimental current in the secondary winding,  $i_p$ , for  $V_i = 40V$

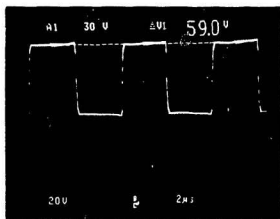


Figure 4.23: Experimental drain to source voltage  $v_{ds}$ , for  $V_i = 60V$

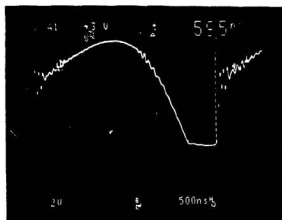


Figure 4.24: Experimental voltage across the diode rectifier,  $v_d$ , for  $V_i = 60V$

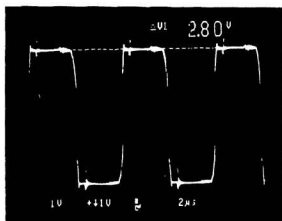


Figure 4.25: Experimental current in the secondary winding,  $i_p'$ , for  $V_i = 60V$

### 4.2.2 Tertiary side resonant converter

This converter is designed to the same specifications as the primary side resonant converter. In addition, this converter also supplies +12V and -12V dc at the output. During the course of this experiment, the  $\pm 12V$  supply was kept at minimum load.

The full-bridge inverter is the same as the one used in the primary side resonant converter. The series branch of the resonant circuit is the same, while the parallel branch is placed on the tertiary winding. The primary to tertiary turns ratio is 1:2 and primary to secondary turns ratio is 4:1. The transformer is made of a ferrite core of horizontal construction. The waveforms shown are for operation at  $V_i = 40V$  and 60V.

Table 4.3 shows the experimental input and output currents and voltages for step-variation in load. Figure 4.26 shows the efficiency of the converter with step variation in load. The figure shows that the efficiency is the highest at about half load. The efficiency is lower for this converter because of the additional  $\pm 12V$  outputs.

Figures 4.27 to 4.38 show the simulated and experimental waveforms and the instantaneous and peak values for  $v_s$ ,  $v_p$ , and the resonant current,  $i_s$ . Figures 4.39 to 4.43 show waveforms of the drain to source voltage of the power switch,  $v_{ds}$ , voltage

Table 4.3: Experimental results showing the variation in efficiency with load for  $V_i = 40V$ , for tertiary side resonance

S. No.	$V_i$ (volts)	$I_i$ (amps)	$V_o$ (volts)	$I_o$ (amps)	$V + 12$ (volts)	$I + 12$ (amps)	$V - 12V$ (volts)	$I - 12V$ (amps)	Eff. %
1.	40.3	1.9	5.12	2.0	11.94	1.6	11.90	2.0	69.41
2.	40.2	4.6	5.12	20.0	11.93	1.6	11.90	2.0	78.57
3.	40.1	7.9	5.12	40.0	11.92	1.6	11.90	2.0	78.19
4.	39.8	11.3	5.13	60.0	11.91	1.6	11.90	2.0	77.97
5.	39.6	14.9	5.13	80.0	11.91	1.6	11.90	2.0	76.82
6.	39.4	18.7	5.13	100.0	11.90	1.6	11.91	2.0	75.44

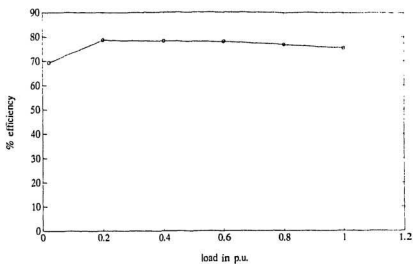


Figure 4.26: Converter efficiency with load,  $V_i = 40V$

across the diode rectifier,  $v_{dr}$ , and voltage across the tertiary winding,  $v_t$ . These waveforms are for operation at two input voltages, 40V and 60V.

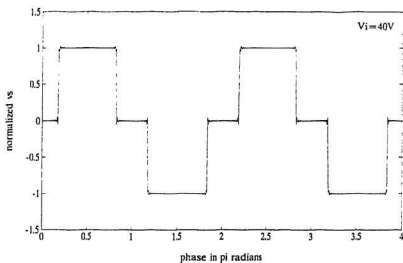


Figure 4.27: Simulated phase shift modulated input voltage,  $v_s$ , for  $V_i = 40V$

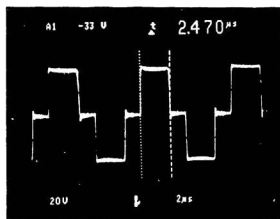


Figure 4.28: Experimental PSM input voltage,  $v_s$ , for  $V_i = 40V$

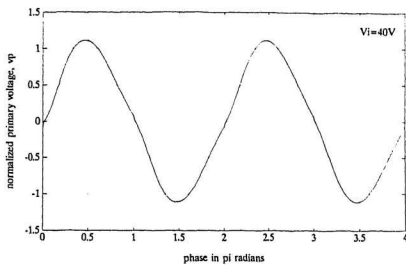


Figure 4.29: Simulated primary voltage,  $v_p$ , for  $V_i = 40V$

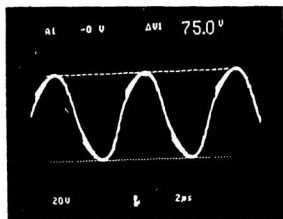


Figure 4.30: Experimental primary voltage,  $v_p$ , for  $V_i = 40V$

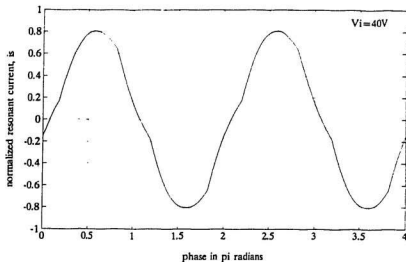


Figure 4.31: Simulated resonant current,  $i_s$ , for  $V_i = 40V$

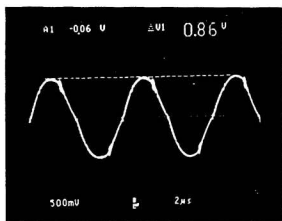


Figure 4.32: Experimental resonant current,  $i_s$ , for  $V_i = 40V$

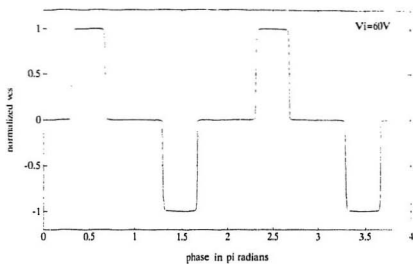


Figure 4.33: Simulated phase shift modulated input voltage,  $v$ , for  $V_i = 60V$

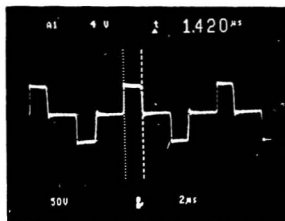


Figure 4.34: Experimental PSM input voltage,  $v$ , for  $V_i = 60V$

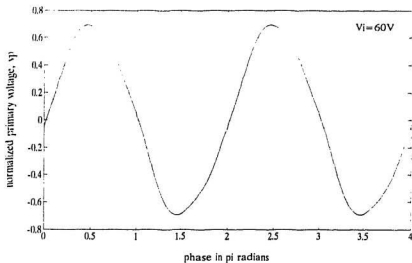


Figure 4.35: Simulated primary voltage,  $v_p$  for  $V_i = 60V$

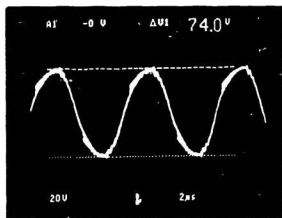


Figure 4.36: Experimental primary voltage,  $v_p$  for  $V_i = 60V$

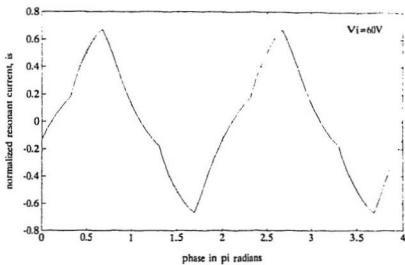


Figure 4.37: Simulated resonant current,  $i_s$ , for  $V_i = 60V$

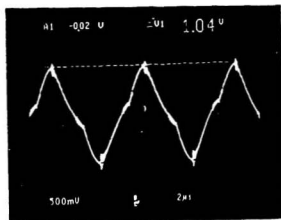


Figure 4.38: Experimental resonant current,  $i_s$ , for  $V_i = 60V$

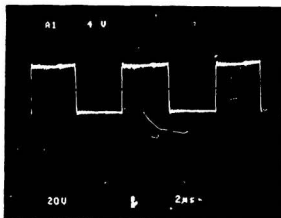


Figure 4.39: Experimental drain to source voltage across one power switch,  $v_{ds}$  for  $V_i = 40V$

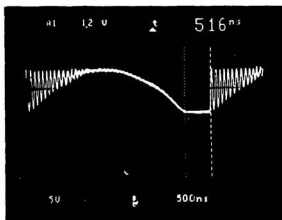


Figure 4.40: Experimental voltage across the diode rectifier,  $v_{dr}$  for  $V_i = 40V$

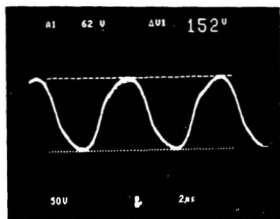


Figure 4.41: Experimental voltage across the tertiary winding,  $v_t$  for  $V_i = 40V$

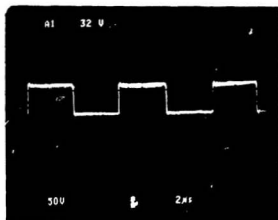


Figure 4.42: Experimental drain to source voltage across one power switch,  $v_{ds}$  for  $V_i = 60V$

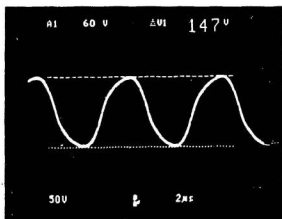


Figure 4.43: Experimental voltage across the tertiary winding,  $v_t$  for  $V_i = 60V$

# Chapter 5

## Conclusion

A generalized frequency-domain model and analysis of dc/dc resonant converters which explicitly takes into account the leakage reactance of the high frequency transformer has been presented in this thesis. The model and analysis procedure can be extended to other dc/dc resonant converter topologies. The model and analysis procedure yields generalized equations which completely describe the performance of the converter for various operating conditions. It is shown that the effect of the leakage inductance of the high frequency transformer is significant and cannot be neglected in converter design.

### 5.1 Summary

The following specific contributions on the modeling and analysis of constant frequency dc/dc resonant converters are made in the thesis.

1. A simplified model of the basic constant frequency dc/dc series-parallel resonant converter incorporating the effect of the transformer leakage inductance has been developed. A steady-state analysis employing harmonic analysis technique and a procedure for determining circuit variables has been outlined. The

resulting expressions are general and can be extended to other resonant dc/dc converter topologies.

2. A frequency-domain model is has also been developed for a constant frequency dc/dc resonant converter with tertiary resonance. This converter is shown to have lower transformer leakage inductance and is therefore found to be more suitable for high frequency operation.
3. Steady-state expressions have been developed to describe the performance of the converters for different operating conditions. Performance curves which are easy to use for the design of the converter have been provided. It is shown that the transformer leakage inductance significantly reduces the output voltage of the converters. This effect is more pronounced at higher frequencies.
4. A transient analysis using the state-space approach has been developed to study the operation of the basic series-parallel resonant converter during the transient period. It is shown that in the transient period, circuit variables can reach as high as three times the steady-state values. However, the circuit operates stably and reaches steady-state in about twenty cycles.
5. Simulated waveforms for steady-state performance have been provided for both converters. Simulation results have been verified by experiments performed on the two types of series-parallel resonant converters. The results confirmed the models and analysis procedure.
6. Modeling and analysis has been presented for the converter with integrated magnetics (i.e., all the magnetic components on the same core). It is shown that integration of magnetics reduces the size of the converter without affecting

it's performance.

7. A design example has been presented to demonstrate the use of performance curves in designing the converter.

## 5.2 Recommendations for further research

The analysis method used in the thesis provides both qualitative and quantitative insight into the steady-state performance and design of the converter. The transient analysis presented in the thesis only provides information on the variation in peak values of the circuit variables during the transient period. The dynamic behaviour and the effect of small perturbations such as changes in width,  $\delta$ , output voltage,  $V_o$  and input voltage,  $V_i$ , on the performance of the converter were not investigated. In order to carry out this investigation, a small-signal model and analysis of the series-parallel converters need to be developed. State-plane representations, discrete-time or sampled data models which provide valuable insight into the dynamics of the circuit and fruitful for evaluating the stability of the cycle-to-cycle behaviour of the circuit need to be developed. The models can also be used to study the acoustic noise generated by the converters.

It has been shown in the thesis that the performance of the converter is not significantly affected by integrated magnetics. However, integrated magnetics presents a design challenge. First, the design of the magnetics has to meet size, weight and losses requirements at high operating frequencies. Second, magnetics have to be optimized to yield high converter efficiency. These issues need further investigation.

## References

- [1] E. Landsman, "A Unifying Derivation of Switching dc-dc Converter Topologies," *IEEE Power Electronics Specialists Conference Record*, 1979, pp. 239-243.
- [2] R. P. Severns and G. Bloom, *Modern DC-to-DC Switchmode Power Converter Circuits*, New York: Van Nostrand Reinhold Co., 1985.
- [3] D. M. Mitchell, *DC-DC Switching Regulator Analysis*, New York: McGraw-Hill, Inc., 1988.
- [4] R. D. Middlebrook and S. Čuk, "A New Optimum Topology Switching dc-to-dc Converter," *IEEE Power Electronics Specialists Conference Record*, 1977, pp. 160-179.
- [5] J. G. Kassakian, M. F. Schlecht and G. C. Verghese, *Principles of Power Electronics*, New York: Addison-Wesley Publishing Company, 1991.
- [6] R. J. King and T. A. Stuart, "A Normalized Model for the Half-Bridge Series Resonant Converters," *IEEE Transactions on Aerospace and Electronics Systems*, Vol. 17, No. 2, March 1981, pp. 190-198.

- [7] R. J. King and T. A. Stuart, "Modeling The Full-Bridge Series-Resonant Power Converter," *IEEE Transactions on Aerospace and Electronic Systems*, Vol.18, no.4, July 1982, pp.449-459.
- [8] V. Volperian and S. Čuk, "A Complete DC Analysis of The Series Resonant Converter," *IEEE Power Electronics Specialists Conference '82 Record*, June 14-17, 1982, pp. 85-100.
- [9] A. F. Witulski and R. W. Erickson, "Steady-State Analysis of the Series Resonant Converter," *IEEE Transactions on aerospace and Electronic Systems*, Vol.21, no.6, November 1985, pp.791-799.
- [10] Ramesh Oruganti and Fred C. Lee, "Resonant Power Processors: Part I - State Plane Analysis," *19th Annual Meeting Conference Record, IEEE Industry Application Society*, 1984, pp. 860-867.
- [11] C. Q. Lee and K. Siri, "Analysis and Design of Series Resonant Converter by State-Plane Diagram," *IEEE Transactions on Aerospace and Electronic Systems*, Vol.22, no.6 November 1986, pp.757-763.
- [12] F. S. Tsai and F. C. Lee, "Constant Frequency Phase Controlled Resonant Power Processors," *IEEE Industry Applications Society Conference Record*, Oct. 1986, pp. 617-622.
- [13] A. K. S. Bhat and S.B. Dewan, "A Generalized Approach for the Steady-State Analysis of Resonant Inverters," *IEEE Transactions on Industry Applications*, Vol.25, No.2, March/April 1989, pp. 326-338.

- [14] V. Vorperian, "Approximate Small-Signal Analysis of the Series and Parallel Resonant Converters," *IEEE Transactions on Power Electronics*, Vol. 6, No. 1, January 1989, pp. 15-24.
- [15] A. F. Witulski, Adán F. Hernandez and R. W. Erickson, "Small Signal Equivalent Circuit Modeling of Resonant Converters," *IEEE Transactions on Power Electronic*, Vol.6,
- [16] J. Ben Klaassens, "Phase-Staggering Control of a Series-Resonant DC-DC converter with Parallel Power Modules," *IEEE Transactions on Power Electronics*, Vol. 3, No. 2, April 1988, pp. 164-173.
- [17] K. D. T. Ngo, "Analysis of a Series Resonant Converter Pulse-width Modulated or Current-Controlled for Low Switching Loss," *IEEE Transactions on Power Electronics*, Vol. 3, No. 1, January 1988.
- [18] Juan A. Sabate, "Off-Line Application of the Fixed-Frequency Clamped-Mode Series Resonant Converter," *IEEE Transactions on Power Electronics*, Vol .6, No. 1, January 1991, pp. 39-47.
- [19] P. Jain, "Performance Comparison of Pulse Width Modulated Resonant Mode DC/DC Converters for Space Applications," *IEEE Industry Applications Society Conference Record*, October 1989, pp. 1106-1114.
- [20] V. T. Ranganathan, P. D. Ziogas and V. R. Stefanovic, "A Regulated DC-DC Voltage Source Converter Using A High Frequency Link," *IEEE Transactions on Industry Application*, Vol. 18, No.3, May/June 1982, pp. 279-287.

- [21] A. K. S. Bhat and S. B. Dewan, "Analysis and Design of a Parallel Resonant Converter Including the Effect of a High-Frequency Transformer," *IEEE Transactions on Industrial Electronics*, Vol. 37, No. 4, August 1990, pp.297-306.
- [22] S. Deb, A. Joshi and S. Doradla, "A Novel Frequency Domain Model for a Parallel Resonant Converter," *IEEE Transaction on Power Electronics*, Vol. 3, No. 2, April 1988, pp. 208-215.
- [23] R. L. Steigerwald, "A Comparison of Half-Bridge Resonant Converter Topologies," *IEEE Transactions on Power Electronics*, Vol. 3, No. 2, April 1988, pp. 174-182.
- [24] A. K. S. Bhat and S. B. Dewan, "Analysis and Design of a High Frequency Resonant Converter Using LCC Type Commutation," *IEEE Industry Applications Society Annual Meeting Conference Record*, 1986, pp.657-663.
- [25] I. Batarseh, R. Liu, C. Q. Lee and A. K. Upadhyay, "150 Watts and 140 kHz Multi-Output LCC-Type Parallel Resonant Converter," *IEEE Applied Power Electronics Conference and Exposition*, 1989, pp. 221-230.
- [26] A. K. S. Bhat, "Fixed Frequency PWM Series-Parallel Resonant Converter," *Industry Applications Society Conference Record*, Oct. 1989, pp. 1115-1121.

- [27] P. Jain, "A Constant Frequency Resonant DC/DC Converter with zero switching Losses," *IEEE Industry Applications Society Conference Record*, October 1991, pp. 1067-1073.
- [28] K. Kuwabara, J. Chida and E. Miyachika, "A Constant Frequency Series-Resonant DC-DC Converter with PWM Controlled Output," *IEEE Power Electronics Specialists Conference Record*, 1988, pp. 563-566.
- [29] Ira J. Pitel, "Phase-Modulated Resonant Power Conversion Techniques for High-Frequency Link Inverters," *IEEE Transactions on Industry Applications*, Vol.22, no.6, November/December 1986, pp.1044-1051.
- [30] F. S. Tsai, P. Materu, and F. C. Lee, "Constant-Frequency, Clamped-Mode Resonant Converters," *IEEE Power Electronics Specialists Conference Record*, 1987, pp. 557-566.
- [31] Pankaj Jain and J. E. Quaicoe, "Generalized Modeling of Constant Frequency DC/DC Resonant Converter Topologies," *IEEE International Telecommunications Energy Conference Record*, 1992, pp. 180-185.







